INTERNATIONAL JOURNAL FOR NUMERICAL METHODS IN ENGINEERING
Int. J. Numer. Meth. Engng 2015; **00**:1–28
Published online in Wiley InterScience (www.interscience.wiley.com). DOI: 10.1002/nme

Linear smoothed polygonal and polyhedral finite elements

Amrita Francis[a], Alejandro Ortiz-Bernardin[b],
Stéphane PA Bordas[c,d,e], Sundararajan Natarajan[a*]

[a]*Department of Mechanical Engineering, Indian Institute of Technology, Madras, Chennai - 600036, India.*
[b]*Department of Mechanical Engineering, University of Chile, Av. Beauchef 851, Santiago, Chile.*
[c] *Faculté des Sciences, de la Technologie et de la Communication, University of Luxembourg, Luxembourg.*
[d]*Theoretical and Applied Mechanics, School of Engineering, Cardiff University, Cardiff CF24 3AA, Wales, UK.*
[e]*Department of Mechanical Engineering, University of Western Australia, Australia.*

SUMMARY

It was observed in [1, 2] that the strain smoothing technique over higher order elements and arbitrary polytopes yields less accurate solutions than other techniques such as the conventional polygonal finite element method. In this work, we propose a linear strain smoothing scheme that improves the accuracy of linear and quadratic approximations over convex polytopes. The main idea is to subdivide the polytope into simplicial subcells and use a linear smoothing function in each subcell to compute the strain. This new strain is then used in the computation of the stiffness matrix. The convergence properties and accuracy of the proposed scheme are discussed by solving a few benchmark problems. Numerical results show that the proposed linear strain smoothing scheme makes the approximation based on polytopes able to deliver the same optimal convergence rate as traditional quadrilateral and hexahedral approximations. The accuracy is also improved, and all the methods tested pass the patch test to machine precision. Copyright © 2015 John Wiley & Sons, Ltd.

Received . . .

KEY WORDS: Smoothed finite element method, linear smoothing, numerical integration, patch test, polytope elements, quadratic serendipity.

1. INTRODUCTION

One of the popular methods for efficient numerical integration in meshfree method is the stablizied conforming nodal integration (SCNI) [3], where the strain field is sampled at the nodes by smoothing the nodal strain on the boundary of a representative nodal volume. In this approach, the nodal strain field is computed by smoothing the standard strain field at the node. Chen et al. [3] showed that the SCNI scheme is more efficient than Gauß integration and passes the linear patch test. Based on this, Liu et al. [4] proposed the smoothed finite element method, which provides a suite of finite elements with a range of interesting properties. Among them are the cell-based SFEM (CSFEM) [5], node based SFEM (NSFEM) [6], edge-based SFEM (ESFEM) [7], face-based SFEM (FSFEM) [8] and alpha-FEM [9]. All these SFEMs use finite element meshes with linear interpolants. A rigorous theoretical framework was provided in [5] and the convergence, stability, accuracy and computational complexity were studied in [10]. The method was also extended to plates [11], shells [12] and nearly incompressible solids [13, 14], and coupled with the extended finite element method [1, 15, 16].

The approach proposed in this paper is closely related to CSFEM. In the CSFEM, the elements are divided into smoothing cells over which the standard (compatible) strain field is smoothed,

*Correspondence to: Department of Mechanical Engineering, Indian Institute of Technology, Madras, Chennai - 600036, India. Email: snatarajan@cardiffalumni.org.uk; snatarajan@iitm.ac.in.

which results in the strain field being computed from the displacement field on the boundary of the smoothing cell. The stiffness matrix is then constructed using this new strain definition and its numerical integration only involves evaluations of few basis functions on the boundary of the smoothing cell—derivatives of basis functions are not needed. It should be noted that the CSFEM employs quadrilateral elements, whereas all other SFEM models usually rely on simplex elements as reference mesh. When the CSFEM is used with linear simplex elements, the resulting stiffness matrix is identical to the conventional FEM. Recently, Natarajan *et al.,* [17] showed the connection between the CSFEM and the virtual element method (VEM) [18, 19, 20, 21]. Dai *et al.,* [22] observed that on an arbitrary polygon with $n > 4$ (where n is the number of sides of the polygon), a minimum of n subcells are required to ensure stability. However, in Reference [2] it was observed that the CSFEM over arbitrary polytopes yields less accurate solutions than other techniques such as the conventional polygonal finite element method [23].

In this paper, we refer to CSFEM as constant smoothing (CS) scheme. Herein, we propose a modification to the CS scheme for arbitrary convex polytopes that leads to improved accuracy and recovers optimal convergence rates. To this end, the polytope is divided into subcells (for instance, triangles/tetrahedra) and by appealing to the recent work of Duan et al. [24, 25, 26], a linear smoothing (LS) scheme is used in each subcell. The subdivision of the polytope into subcells is solely for the purpose of computing the linear smoothed strain and does not add new degrees of freedom to the system.

Section 2 summarizes the governing equations for the linear elastostatics problem. A brief discussion about shape functions over arbitrary convex polygons is given in Section 3. Section 4 presents the construction of the stiffness matrix for polytopes using strain smoothing, where the linear strain smoothing scheme is presented. The efficacy, the convergence properties and the accuracy of the proposed LS scheme for polytopes are studied in Section 5 by solving a few benchmark problems in two- and three-dimensional linear elastostatics. The results from the proposed scheme are compared with conventional cell-based smoothed finite element method. Major conclusions and scope for future work are discussed in the last section.

2. GOVERNING EQUATIONS

Consider an elastic body that occupies the open domain $\Omega \subset \mathbb{R}^d$ and is bounded by the $(d-1)$-dimensional surface Γ whose unit outward normal is $\mathbf{n}$. The boundary is assumed to admit decompositions $\Gamma = \Gamma_u \cup \Gamma_t$ and $\emptyset = \Gamma_u \cap \Gamma_t$, where Γ_u is the Dirichlet boundary and Γ_t is the Neumann boundary. The closure of the domain is $\overline{\Omega} \equiv \Omega \cup \Gamma$. Let $\mathbf{u} : \Omega \to \mathbb{R}^d$ be the displacement field at a point $\mathbf{x}$ of the elastic body when the body is subjected to external tractions $\bar{\mathbf{t}} : \Gamma_t \to \mathbb{R}^d$ and body forces $\mathbf{b} : \Omega \to \mathbb{R}^d$. The imposed Dirichlet (essential) boundary conditions are $\hat{\mathbf{u}} : \Gamma_u \to \mathbb{R}^d$. The boundary-value problem for linear elastostatics is: find $\mathbf{u} : \Omega \to \mathbb{R}^d$ such that

$$\forall \mathbf{x} \in \Omega \quad \boldsymbol{\nabla} \cdot \boldsymbol{\sigma} + \mathbf{b} = 0, \tag{1a}$$

$$\forall \mathbf{x} \in \Gamma_u \quad \mathbf{u} = \hat{\mathbf{u}}, \tag{1b}$$

$$\forall \mathbf{x} \in \Gamma_t \quad \boldsymbol{\sigma} \cdot \mathbf{n} = \hat{\mathbf{t}}, \tag{1c}$$

where $\boldsymbol{\sigma}$ is the Cauchy stress tensor. The corresponding weak form is: find $\mathbf{u} \in \mathscr{U}$ such that

$$\forall \mathbf{v} \in \mathscr{V}, \quad a(\mathbf{u}, \mathbf{v}) = \ell(\mathbf{v}) \tag{2a}$$

$$a(\mathbf{u}, \mathbf{v}) = \int_\Omega \boldsymbol{\sigma}(\mathbf{u}) : \boldsymbol{\varepsilon}(\mathbf{v}) \, \mathrm{d}V, \quad \ell(\mathbf{v}) = \int_\Omega \mathbf{b} \cdot \mathbf{v} \, \mathrm{d}V + \int_{\Gamma_t} \hat{\mathbf{t}} \cdot \mathbf{v} \, \mathrm{d}S, \tag{2b}$$

where $\boldsymbol{\varepsilon}$ is the small strain tensor, and $\mathscr{U}$ and $\mathscr{V}$ are the displacement trial and test spaces:

$$\mathscr{U} := \left\{ \mathbf{u}(\mathbf{x}) \in [C^0(\Omega)]^d : \mathbf{u} \in [\mathcal{W}(\Omega)]^d \subseteq [H^1(\Omega)]^d, \ \mathbf{u} = \hat{\mathbf{u}} \text{ on } \Gamma_u \right\},$$

$$\mathscr{V} := \left\{ \mathbf{v}(\mathbf{x}) \in [C^0(\Omega)]^d : \mathbf{v} \in [\mathcal{W}(\Omega)]^d \subseteq [H^1(\Omega)]^d, \ \mathbf{v} = \mathbf{0} \text{ on } \Gamma_u \right\},$$

DOI: 10.1002/nme

where the space $\mathcal{W}(\Omega)$ includes linear displacement fields. The domain is partitioned into elements Ω^h, and on using shape functions ϕ_a that span at least the linear space, we substitute vector-valued trial and test functions $\mathbf{u}^h = \sum_a \phi_a \mathbf{u}_a$ and $\mathbf{v}^h = \sum_b \phi_b \mathbf{v}_b$, respectively, into Equation (2) and apply a standard Galerkin procedure to obtain the discrete weak form: find $\mathbf{u}^h \in \mathscr{U}^h$ such that

$$\forall \mathbf{v}^h \in \mathscr{V}^h \quad a(\mathbf{u}^h, \mathbf{v}^h) = \ell(\mathbf{v}^h), \tag{4}$$

which leads to the following system of linear equations:

$$\mathbf{K}\mathbf{u} = \mathbf{f}, \tag{5a}$$

$$\mathbf{K} = \sum_h \mathbf{K}^h = \sum_h \int_{\Omega^h} \mathbf{B}^{\mathrm{T}} \mathbf{C} \mathbf{B} \, \mathrm{d}V, \tag{5b}$$

$$\mathbf{f} = \sum_h \mathbf{f}^h = \sum_h \left(\int_{\Omega^h} \mathbf{N}^{\mathrm{T}} \mathbf{b} \, \mathrm{d}V + \int_{\Gamma_t^h} \mathbf{N}^{\mathrm{T}} \hat{\mathbf{t}} \, \mathrm{d}S \right), \tag{5c}$$

where $\mathbf{K}$ is the assembled stiffness matrix, $\mathbf{f}$ the assembled nodal force vector, $\mathbf{u}$ the assembled vector of nodal displacements, $\mathbf{N}$ is the matrix of shape functions, $\mathbf{C}$ is the constitutive matrix for an isotropic linear elastic material, and $\mathbf{B} = \boldsymbol{\nabla}_s \mathbf{N}$ is the strain-displacement matrix that is computed using the derivatives of the shape functions.

The shape functions over arbitrary polygons/polyhedra are collectively called as 'barycentric coordinates'. Because there is no unique way to represent the shape functions over polytopes, there are multiple approaches to construct them. Interested readers are referred to Reference [27] for a detailed discussion on the construction of shape functions over polytopes. In this paper, Wachspress interpolants are used [28].

The main issue in computing the stiffness matrix defined in Equation (5) for polygonal/polyhedral elements is the construction of sufficiently accurate integration rules. In an effort to improve the accuracy, a modified version of the strain-displacement matrix is usually defined to compute the stiffness matrix. This modified strain-displacement matrix is denoted by $\tilde{\mathbf{B}}$ and is constructed using smoothing domains that produce constant strains in the polygonal/polyhedral element. A smoothing technique that yields linear strains and improved accuracy in polygonal/polyhedral finite elements is proposed in this paper. Thus,the stiffness matrix is computed as for the constant smoothing:

$$\tilde{\mathbf{K}} = \sum_h \tilde{\mathbf{K}}^h = \sum_h \int_{\Omega^h} \tilde{\mathbf{B}}^{\mathrm{T}} \mathbf{C} \tilde{\mathbf{B}} \, \mathrm{d}V, \tag{6}$$

This is also true for linear smoothing technique, where only the matrix $\tilde{\mathbf{B}}$ varies, with a linear smoothed strain-displacement operator (see Section 4.2) as opposed to a constant smoothed strain-displacement operator (see Section 4.1) [4, 17].

3. SHAPE FUNCTIONS FOR ARBITRARY CONVEX POLYTOPES

In this section, shape functions employed over arbitrary convex polygons and polyhedron are discussed. A brief overview of shape functions that are linear on the element boundary is given, followed by quadratic serendipity shape functions over arbitrary convex polygons.

3.1. Wachspress interpolants

Wachspress [29], by using the principles of perspective geometry, proposed rational basis functions on polygonal elements, in which the algebraic equations of the edges are used to ensure nodal interpolation and linearity on the boundaries. A discussion on their use for smoothed polygonal elements is given in [28]. In Reference [30], a simple expression is obtained for Wachspress shape

Prepared using nmeauth.cls
DOI: 10.1002/nme

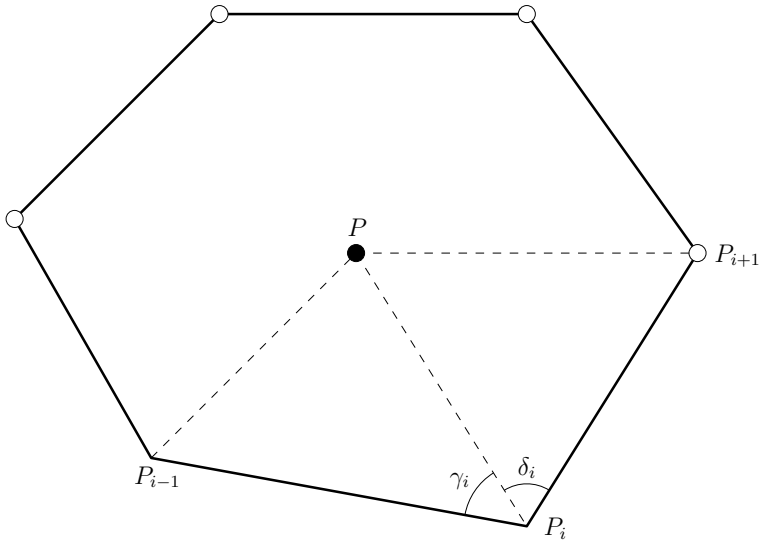

Figure 1. Barycentric coordinates: Wachspress basis function

functions, as follows:

$$\phi_i^w(\mathbf{x}) = \frac{w_i(\mathbf{x})}{\sum_{j=1}^n w_j(\mathbf{x})}, \tag{7}$$

$$w_i(\mathbf{x}) = \frac{A(p_{i-1}, p_i, p_{i+1})}{A(p_{i-1}, p_i, p)A(p_i, p_{i+1}, p)} = \frac{\cot\gamma_i + \cot\delta_i}{||\mathbf{x} - \mathbf{x}_i||^2}, \tag{8}$$

where $A(a, b, c)$ is the signed area of triangle $[a, b, c]$, and γ_i and δ_i are shown in Figure 1. The generalization of Wachspress shape functions to simplex convex polyhedra was given by Warren [31, 32]. The construction of the coordinates is as follows: Let $P \subset \mathbb{R}^3$ be a simple convex polyhedron with facets F and vertices V. For each facet $f \in F$, let $\mathbf{n}_f$ be the unit outward normal and for any $\mathbf{x} \in P$, let $h_f(\mathbf{x})$ denote the perpendicular distance of $\mathbf{x}$ to f, which is given by

$$h_f(\mathbf{x}) = (\mathbf{v} - \mathbf{x}) \cdot \mathbf{n}_f \tag{9}$$

for any vertex $\mathbf{v} \in V$ that belongs to f. For each vertex $\mathbf{v} \in V$, let f_1, f_2, f_3 be the three faces incident to $\mathbf{v}$ and for $\mathbf{x} \in P$, let

$$w_{\mathbf{v}}(\mathbf{x}) = \frac{\det(\mathbf{n}_{f_1}, \mathbf{n}_{f_2}, \mathbf{n}_{f_3})}{h_{f_1}(\mathbf{x})h_{f_2}(\mathbf{x})h_{f_3}(\mathbf{x})}. \tag{10}$$

The shape functions for $\mathbf{x} \in P$ is then given by

$$\phi_{\mathbf{v}}(\mathbf{x}) = \frac{w_{\mathbf{v}}(\mathbf{x})}{\sum\limits_{\mathbf{u}\in V} w_{\mathbf{u}}(\mathbf{x})}. \tag{11}$$

The Wachspress shape functions are the lowest order shape functions that satisfy boundedness, linearity and linear consistency on convex polyshapes [31, 32].

3.2. Quadratic serendipity shape functions

Rand *et al.,* [33] presented a simple construction of shape functions over arbitrary convex polygons that have a quadratic rate of convergence. This extends the work on serendipity elements to arbitrary polygons/polyhedron, which were earlier restricted to quadrilateral (for instance, 8-noded serendipity) and hexahedral elements (for instance, 20 noded serendipity brick element). The essential steps involved in the construction of quadratic serendipity shape functions are pictorially shown in Figure 2 and are [33]:

DOI: 10.1002/nme

1. Select a set of barycentric coordinates $\phi_i, i = 1, \cdots, n$, where n is the number of vertices of the polygon.
2. Compute pairwise functions $\mu_{ab} := \phi_a \phi_b$. This construction yields a total of $n(n+1)/2$ functions.
3. Apply a linear transformation $\mathbb{A}$ to μ_{ab}. The linear transformation $\mathbb{A}$ reduces the set μ_{ab} to $2n$ set of functions ξ_{ij} indexed over vertices and edge midpoints of the polygon.
4. Apply another linear transformation $\mathbb{B}$ that converts ξ_{ij} into a basis ψ_{ij} which satisfies the "Lagrange property."

In the present study, Wachspress interpolants are selected to represent the barycentric coordinates ϕ_i. Instead of using a single 'reference' element, Rand *et al.,* [33], proposed to analyse classes of 'reference' elements, namely, diameter one convex polygons. The transformation matrix $\mathbb{A}$ that reduces the set μ_{ab} has the following structure:

$$\mathbb{A} := [\ \mathbb{I}\ |\ \mathbb{A}'\ ], \tag{12}$$

where $\mathbb{I}$ is the $2n \times 2n$ identity matrix and each column in $\mathbb{A}'$ corresponds to the relation between the interior diagonal of the pairwise product basis with the midpoints of boundary edges. The pairwise functions set μ_{ab} and the reduced basis set are related by

$$\xi_{ij} = \mathbb{A}\mu_{ab}. \tag{13}$$

The pairwise products are grouped with the following specific basis orderings: $\mu_{ab} = [\underbrace{\mu_{11}, \cdots, \mu_{nn}}_{\text{indices in V}}, \underbrace{\mu_{12}, \cdots, \mu_{n(n+1)}}_{\text{indices in E}}, \underbrace{\mu_{13}, \cdots, \mu_{(n-2)n}}_{\text{indices in D}}]$., where V, E and D corresponds to the geometrical features of the polygon, namely, vertices, edges of the boundary and the interior diagonals, respectively. The transformation matrix $\mathbb{B}$ is given by

$$\mathbb{B} = \left[\begin{array}{ccc|ccc} 1 & & & -1 & \cdots & -1 \\ & 1 & & -1 & -1 & \cdots \\ & & \ddots & & \ddots & \ddots \\ & & 1 & & -1 & -1 \\ \hline & & & 4 & & \\ & 0 & & & 4 & \\ & & & & & \ddots \\ & & & & & 4 \end{array}\right]. \tag{14}$$

The above transformation matrix, converts the serendipity shape functions to ψ_{ij} that satisfies the "Lagrange property," i.e.,

$$\psi_{ij} = \mathbb{B}\xi_{ij}. \tag{15}$$

Interested readers are referred to Reference [33] for a detailed discussion on the construction of the linear transformation matrices $\mathbb{A}$ and $\mathbb{B}$. Figure 3 shows one of the barycentric coordinates of a pentagon and the quadratic shape function. The intermediate shape function ξ_I is also shown to not possess the Kronecker delta property.

4. STIFFNESS MATRIX FOR POLYTOPES USING STRAIN SMOOTHING

The next step in the process is to compute the modified strain-displacement matrix to build the stiffness matrix Equation (6). To this end we rely on the smoothed finite element method (SFEM), which has its origin in the stabilized conforming nodal integration (SCNI) [3] for meshfree methods, where the strain field is sampled at the nodes by smoothing the nodal strain on the boundary of a

DOI: 10.1002/nme

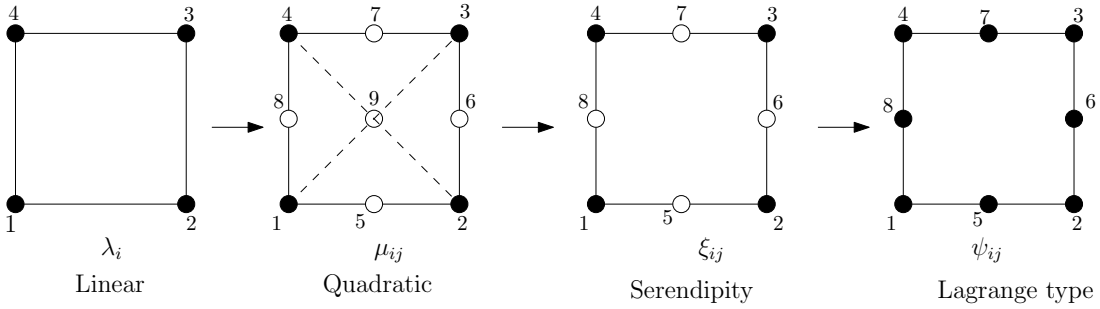

Figure 2. Construction of quadratic serendipity shape functions based on generalized barycentric coordinates.

representative nodal volume ('the smoothed domain'). In particular, we focus our attention on the cell-based smoothing technique. In the CSFEM, the elements are divided into subcells as shown in Figure 4. In this paper, we use triangles in two dimensions and tetrahedra in three dimensions. The strain smoothing technique is then applied within each subcell to evaluate the modified strain. For simplicity of the notation, the derivation of the smoothing scheme is given in detail only for two-dimensions. The Cartesian coordinate system is chosen, where for convenience $x \equiv x_1$ and $y \equiv x_2$. In addition, n_j $(j = 1, 2)$ is the j-th component of the unit outward normal to a cell edge in the Cartesian coordinate system. The discrete strain field $\tilde{\varepsilon}^h_{ij}$ that yields the modified strain-displacement matrix $\tilde{\mathbf{B}}$ that is used to build the stiffness matrix is computed by a weighted average of the standard strain field ε^h_{ij} in each subcell Ω^h_C, as follows:

$$\tilde{\varepsilon}^h_{ij}(\mathbf{x}) = \int_{\Omega^h_C} \varepsilon^h_{ij}(\mathbf{x}) f(\mathbf{x}) \mathrm{d}V, \tag{16}$$

where f is a smoothing function. On writing Equation (16) at the basis functions derivatives level, its right-hand side can be expressed in terms of the divergence theorem, as follows:

$$\int_{\Omega^h_C} \phi_{a,j} f(\mathbf{x})\, \mathrm{d}V = \int_{\Gamma^h_C} \phi_a f(\mathbf{x}) n_j\, \mathrm{d}S - \int_{\Omega^h_C} \phi_a f_{,j}(\mathbf{x})\, \mathrm{d}V. \tag{17}$$

Equation (17) was coined as *divergence consistency* in Duan et al. [24, 25, 26], where it was introduced to correct integration errors in second- and third-order meshfree approximations. This divergence consistency was later used by Sukumar to correct integration errors in quadratic maximum-entropy serendipity polygonal elements [34] and by Ortiz-Bernardin and co-workers to correct integration errors in the volume-averaged nodal projection (VANP) meshfree method [35, 36].

To obtain the modified strain-deformation matrix for the polygonal element, Equation (17) is solved through Gauß integration, which leads to a system of linear equations where the values of the shape functions derivatives evaluated at the m-th integration point (denoted by ${}^m\mathbf{r}$) in the interior of the subcell, namely $\phi_{a,j}({}^m\mathbf{r})$, are the unknowns. In this process, only basis functions are involved—derivatives of basis functions are not needed. This effectively means that the interior derivatives are replaced by modified derivatives that are computed based on the shape functions. The modified derivatives are then used to compute the discrete modified strain. Thus, at the m-th integration point in the interior of the subcell Ω^h_C, the discrete modified strain is

$$\tilde{\varepsilon}^h({}^m\mathbf{r}) = \tilde{\mathbf{B}}({}^m\mathbf{r})\mathbf{q}, \tag{18}$$

where $\mathbf{q}$ contains unknown nodal displacements that belong to the element. The number of interior integration points that are required per subcell is related to the number of terms in the smoothing function f and will be discussed later (see Remark 1). The smoothed element stiffness matrix for

DOI: 10.1002/nme

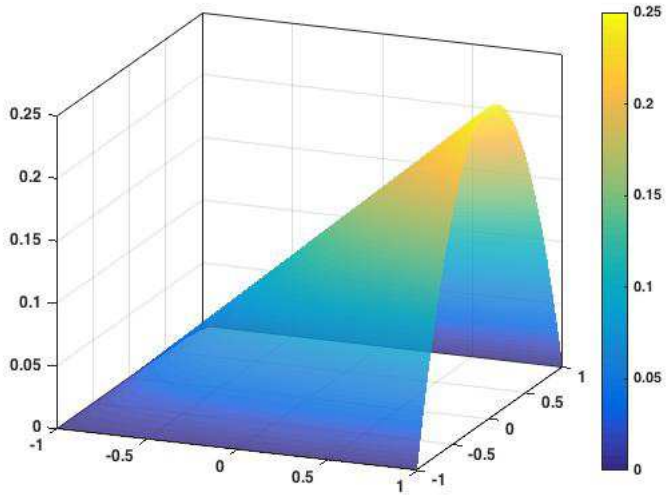

(a) Serendipity shape function (ξ) without the "Lagrange property".

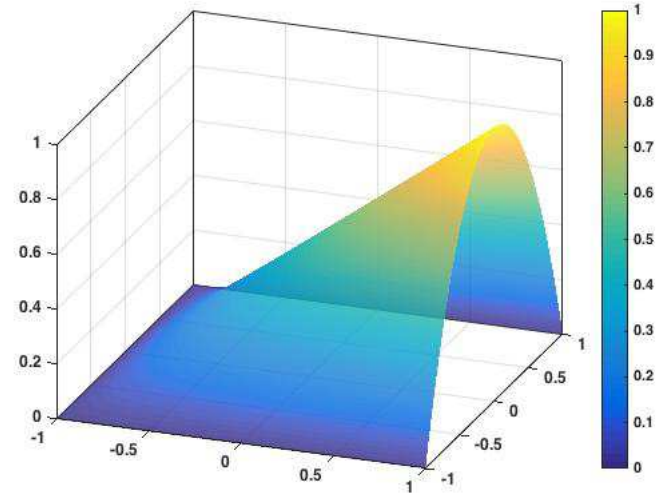

(b) Serendipity shape function (ψ) with the "Lagrange property".

Figure 3. Quadratic serendipity shape functions for quadrilateral element. The shape function for node 6 (see Figure 2) is shown. Note that the function ξ does not possess the Kronecker delta property. After applying the transformation matrix $\mathbb{B}$, the serendipity shape function at node 6 possess the Kronecker delta property.

the element h is computed by the sum of the contributions of the subcells as

$$\tilde{\mathbf{K}}^h = \sum_{C=1}^{nc} \left(\sum_{m=1}^{ngp} \tilde{\mathbf{B}}^{\mathrm{T}}({}^m\mathbf{r}) \mathbf{C} \tilde{\mathbf{B}}({}^m\mathbf{r}) w_m \right) \tag{19}$$

where nc is the number of subcells of the element, ngp the number of Gauß points per subcell and w_m are the integration weights. Two particular smoothing functions along with their associated modified strain-displacement matrices are discussed next.

DOI: 10.1002/nme

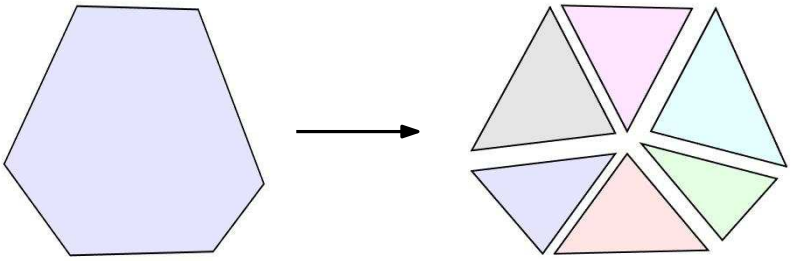

(a) 2D: subdivision into triangles

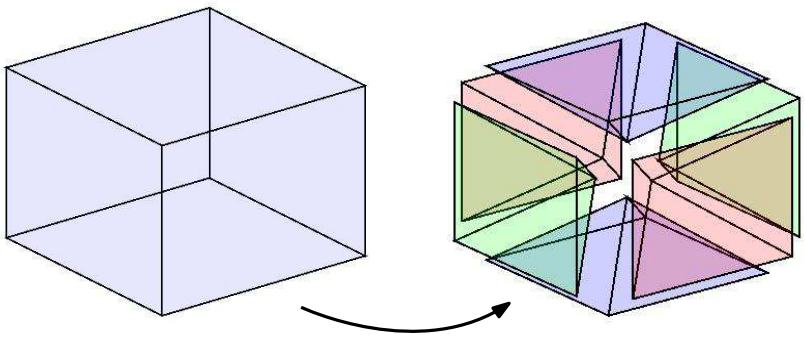

(b) 3D: subdivision into pentahedron

Figure 4. Representative subdivision of an element into subcells: (a) arbitrary polygon (b) hexahedron. Note that the polygon/polyhedron can be subdivided into subcells of any shape. However, for simplicity we employ triangles in two dimensions and tetrahedra in three dimensions.

4.1. Constant smoothing

In the conventional cell-based smoothing technique, which we refer to as constant smoothing (CS) scheme, the smoothing function f is chosen to be a constant, i.e.,

$$f(\mathbf{x}) = 1, \tag{20}$$

whose derivative is $f_{,j}(\mathbf{x}) = 0, \forall x$ in the subcell. Herein, this is referred to as constant smoothing. One interior Gauß point ($ngp = 1$) per subcell is required to compute the smoothed element stiffness matrix Equation (19). Thus in two dimensions, Equation (17) leads to

$$\phi_{a,1} = \frac{1}{A_C} \int_{\Gamma_C^h} \phi_a(\mathbf{x}) n_1 \, \mathrm{d}S, \tag{21a}$$

$$\phi_{a,2} = \frac{1}{A_C} \int_{\Gamma_C^h} \phi_a(\mathbf{x}) n_2 \, \mathrm{d}S, \tag{21b}$$

which for a polygon of n sides, gives the following expression for the modified strain-displacement matrix evaluated at the interior Gauß point:

$$\tilde{\mathbf{B}} = \left[\begin{array}{cccc} \tilde{\mathbf{B}}_1 & \tilde{\mathbf{B}}_2 & \cdots & \tilde{\mathbf{B}}_n \end{array} \right], \tag{22}$$

DOI: 10.1002/nme

where the nodal matrix is

$$\tilde{\mathbf{B}}_a = \frac{1}{A_C}\int_{\Gamma_C^h} \begin{bmatrix} n_1 & 0 \\ 0 & n_2 \\ n_2 & n_1 \end{bmatrix} \phi_a(\mathbf{x})\mathrm{d}S \tag{23}$$

with A_C being the area of the subcell. Similarly, in three dimensions the expression for the nodal matrix is

$$\tilde{\mathbf{B}}_a = \frac{1}{V_C}\int_{\Gamma_C^h} \begin{bmatrix} n_1 & 0 & 0 \\ 0 & n_2 & 0 \\ 0 & 0 & n_3 \\ n_2 & n_1 & 0 \\ 0 & n_3 & n_2 \\ n_3 & 0 & n_1 \end{bmatrix} \phi_a(\mathbf{x})\mathrm{d}S \tag{24}$$

with V_C being the volume of the subcell.

Within this framework, the constant smoothing technique could be used without subdividing the element into subcells. Figure 5 shows a schematic representation of the constant smoothing technique over a hexagon. Note that because of the choice of the smoothing function f, various choices of subcells are possible. The smoothing can be performed over the entire element (also referred to as one subcell in the literature) or over each of the sub-triangles. Natarajan *et al.* [17], established a connection between the one subcell version of the smoothing technique and the recently proposed virtual element method [37].

Remark 1

When constant smoothing is performed over the entire element, a stabilization term is required to eliminate additional spurious energy modes [4, 10, 17].

4.2. *Linear smoothing*

In the proposed linear smoothing (LS) scheme, the smoothing function f is the linear polynomial basis

$$f(\mathbf{x}) = [1 \;\; x_1 \;\; x_2]^{\mathrm{T}}, \tag{25}$$

whose derivative (δ_{ij} is the Kronecker delta symbol) is

$$f_{,j}(\mathbf{x}) = [0 \;\; \delta_{1j} \;\; \delta_{2j}]^{\mathrm{T}}. \tag{26}$$

In two dimensions, the expanded version of Equation (17) is

$$\int_{\Omega_C^h} \phi_{a,1}\,\mathrm{d}V = \int_{\Gamma_C^h} \phi_a n_1\,\mathrm{d}S, \tag{27a}$$

$$\int_{\Omega_C^h} \phi_{a,1}x_1\,\mathrm{d}V = \int_{\Gamma_C^h} \phi_a x_1 n_1\,\mathrm{d}S - \int_{\Omega_C^h} \phi_a\,\mathrm{d}V, \tag{27b}$$

$$\int_{\Omega_C^h} \phi_{a,1}x_2\,\mathrm{d}V = \int_{\Gamma_C^h} \phi_a x_2 n_1\,\mathrm{d}S, \tag{27c}$$

for $\phi_{a,1}$, and

$$\int_{\Omega_C^h} \phi_{a,2}\,\mathrm{d}V = \int_{\Gamma_C^h} \phi_a n_2\,\mathrm{d}S, \tag{27d}$$

$$\int_{\Omega_C^h} \phi_{a,2}x_1\,\mathrm{d}V = \int_{\Gamma_C^h} \phi_a x_1 n_2\,\mathrm{d}S, \tag{27e}$$

$$\int_{\Omega_C^h} \phi_{a,2}x_2\,\mathrm{d}V = \int_{\Gamma_C^h} \phi_a x_2 n_2\,\mathrm{d}S - \int_{\Omega_C^h} \phi_a\,\mathrm{d}V \tag{27f}$$

for $\phi_{a,2}$.

DOI: 10.1002/nme

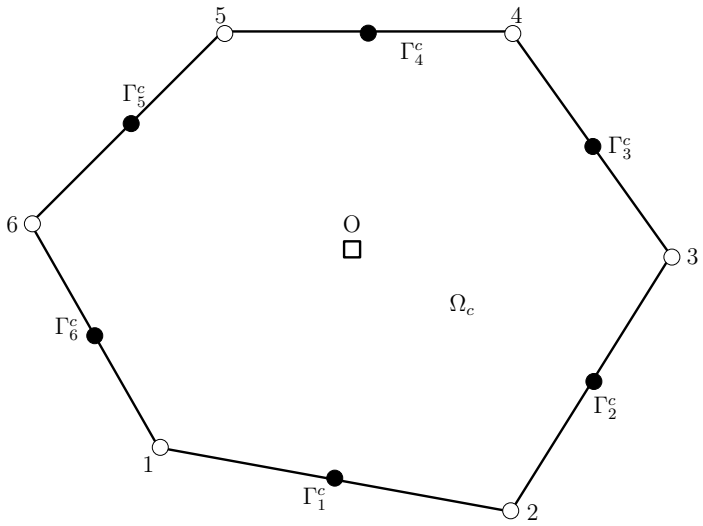

(a) No subdivision into triangles

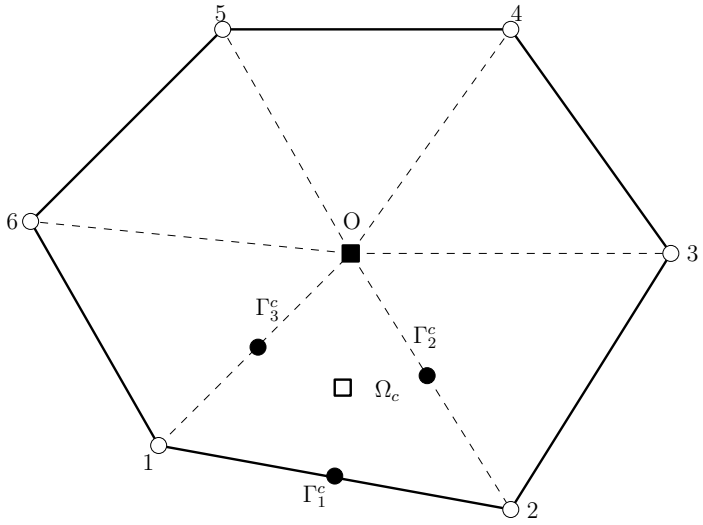

(b) subdivision into triangles

Figure 5. Schematic representation of the constant smoothing technique. The interior Gauß points are depicted as 'open' squares, while the Gauß points on the cell's edges are shown as 'filled' circles. The white nodes are the nodes of the element. The modified derivatives are computed at the 'open' squares.

Subcells are used to integrate Equation (27) (in the proposed method, we use triangular subcells). A representative polygon and its integration subcells are shown in Figure 6. Let the coordinates of the m-th interior subcell Gauß point be defined as ${}^m\mathbf{r} = ({}^mr_1, {}^mr_2)$ and its associated Gauß weight as ${}^mw$; the coordinates and the Gauß weight of the g-th Gauß point that is located on the k-th edge of the subcell is ${}^g_k\mathbf{s} = ({}^g_ks_1, {}^g_ks_2)$ and ${}^g_kv$, respectively; and the unit outward normal to the k-th edge of the subcell is denoted by ${}_k\mathbf{n} = ({}_kn_1, {}_kn_2)$. In two dimensions, three interior Gauß points ($ngp = 3$) per subcell are required to compute the smoothed element stiffness matrix Equation (19). Using numerical integration in Equation (27) leads to the following system of linear equations:

$$\mathbf{W}\mathbf{d}_j = \mathbf{f}_j, \quad j = 1, 2 \tag{28a}$$

DOI: 10.1002/nme

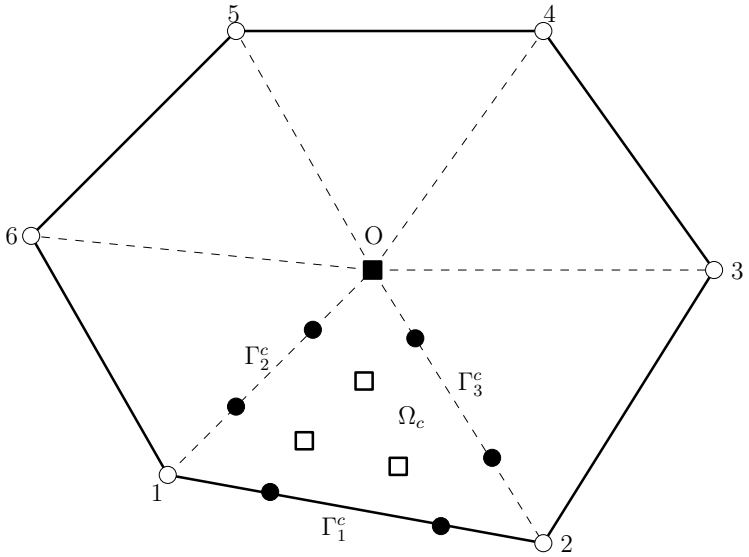

Figure 6. Schematic representation of a two-dimensional sub-triangulation for the linear smoothing scheme. The geometric center of the polygon is used to sub-triangulate the polygon. The interior Gauß points are depicted as 'open' squares, while the Gauß points on the cell's edges are shown as 'filled' circles. The white nodes are the nodes of the element. Note that the center of the polygon does not introduce an additional node. It is introduced solely for the purpose of integration. The modified derivatives are computed at the 'open' squares.

where

$$\mathbf{W} = \begin{bmatrix} {}^1w & {}^2w & {}^3w \\ {}^1w\,{}^1x_1 & {}^2w\,{}^2x_1 & {}^3w\,{}^3x_1 \\ {}^1w\,{}^1x_2 & {}^2w\,{}^2x_2 & {}^3w\,{}^3x_2 \end{bmatrix}, \tag{28b}$$

$$\mathbf{f}_1 = \begin{bmatrix} \sum_{k=1}^{3}\sum_{g=1}^{2} \phi_a({}^g_k\mathbf{s})\,{}_kn_1\,{}^g_kv \\ \sum_{k=1}^{3}\sum_{g=1}^{2} \phi_a({}^g_k\mathbf{s})\,{}^g_ks_1\,{}_kn_1\,{}^g_kv - \sum_{m=1}^{3} \phi_a({}^m\mathbf{r})\,{}^mw \\ \sum_{k=1}^{3}\sum_{g=1}^{2} \phi_a({}^g_k\mathbf{s})\,{}^g_ks_2\,{}_kn_1\,{}^g_kv \end{bmatrix}, \tag{28c}$$

$$\mathbf{f}_2 = \begin{bmatrix} \sum_{k=1}^{3}\sum_{g=1}^{2} \phi_a({}^g_k\mathbf{s})\,{}_kn_2\,{}^g_kv \\ \sum_{k=1}^{3}\sum_{g=1}^{2} \phi_a({}^g_k\mathbf{s})\,{}^g_ks_1\,{}_kn_2\,{}^g_kv \\ \sum_{k=1}^{3}\sum_{g=1}^{2} \phi_a({}^g_k\mathbf{s})\,{}^g_ks_2\,{}_kn_2\,{}^g_kv - \sum_{m=1}^{3} \phi_a({}^m\mathbf{r})\,{}^mw \end{bmatrix}, \tag{28d}$$

and the solution vector of the j-th basis function derivative evaluated at the three interior subcell Gauß points is

$$\mathbf{d}_j = \begin{bmatrix} {}^1d_j & {}^2d_j & {}^3d_j \end{bmatrix} = \begin{bmatrix} \phi_{a,j}({}^1\mathbf{r}) & \phi_{a,j}({}^2\mathbf{r}) & \phi_{a,j}({}^3\mathbf{r}) \end{bmatrix}^{\mathrm{T}}. \tag{28e}$$

In the preceding equations, the index a runs through the nodes that define the polygonal element. For a polygon of n sides, the modified derivatives given in Equation (28e) are used to evaluate the modified strain-displacement matrix at the interior subcell Gauß points, as follows:

$$\tilde{\mathbf{B}}({}^k\mathbf{r}) = \begin{bmatrix} \tilde{\mathbf{B}}_1({}^k\mathbf{r}) & \tilde{\mathbf{B}}_2({}^k\mathbf{r}) & \cdots & \tilde{\mathbf{B}}_n({}^k\mathbf{r}) \end{bmatrix}, \; k = 1, 2, 3, \tag{29}$$

DOI: 10.1002/nme

where the nodal matrix evaluated at the k-th interior subcell Gauß point is

$$\tilde{\mathbf{B}}_a({}^k\mathbf{r}) = \begin{bmatrix} {}^kd_1 & 0 \\ 0 & {}^kd_2 \\ {}^kd_2 & {}^kd_1 \end{bmatrix} \tag{30}$$

Remark 2
For the LS scheme, the arbitrary convex polygonal/polyhedral element is always sub-divided into triangles (in two dimensions) and tetrahedra (in three dimensions). The LS scheme is then applied over each subdivision (subcell). This is done because the number of interior Gauß points needed to integrate in Equation (27) is exactly the number of terms in the smoothing function. However, for the 4-node quadrilateral element, we choose $f(\mathbf{x}) = [1 \;\; x_1 \;\; x_2 \;\; x_1x_2]^{\mathrm{T}}$ and because a four-point Gauß quadrature rule is available for this element, the sub-division is not performed. In this case, we could refer to it as 'bilinear smoothing.'

Finally, for a polyhedron the subcell is a tetrahedron and the smoothing procedure can be derived from the linear basis

$$f(\mathbf{x}) = [1 \;\; x_1 \;\; x_2 \;\; x_3]^{\mathrm{T}}, \tag{31}$$

and its derivative

$$f_{,j}(\mathbf{x}) = [0 \;\; \delta_{1j} \;\; \delta_{2j} \;\; \delta_{3j}]^{\mathrm{T}}. \tag{32}$$

The corresponding triangular/tetrahedral quadratures that are used in the smoothing scheme for both the interior and edge/face Gauß points are provided in Appendix A.

5. NUMERICAL EXAMPLES

In this section, we demonstrate the accuracy and convergence properties of the proposed linear smoothing scheme (LS) to compute the shape function derivatives in polygonal and polyhedral finite elements. The LS scheme is compared to the usual constant smoothing (CS) scheme by solving few benchmark problems. We also demonstrate the performance of the scheme in a simple three-dimensional elasticity problem. In all the numerical examples, we discretize the domain with arbitrary polytope based on centroid Voronoi tessellation. The following convention is used while discussing the results:

- CS-Q4, LS-Q4: constant and linear smoothing scheme over 4-noded quadrilateral element, respectively.
- LS-Q8: linear smoothing scheme over 8-noded quadrilateral serendipity element.
- LS-H8: linear smoothing scheme over 8-noded hexahedral element.
- CS-Poly2D (linear), LS-Poly2D (linear): constant and linear smoothing scheme over arbitrary polygons, respectively.
- CS-Poly2D (quadratic), LS-Poly2D (quadratic) - constant and linear smoothing scheme over arbitrary serendipity polygons, respectively.
- LS-Poly3D - linear smoothing scheme over arbitrary polyhedron.

Table I lists the type and the order of approximation functions employed for various element types considered in this study. For the purpose of error estimation and convergence studies, the L^2 norm and H^1 seminorm of the error are used.

5.1. Linear patch test

In the first example, the accuracy of the proposed LS scheme is demonstrated with a linear patch test. The following displacements are prescribed on the boundary in the two-dimensional case:

$$\begin{pmatrix} \hat{u} \\ \hat{v} \end{pmatrix} = \begin{pmatrix} 0.1 + 0.1x + 0.2y \\ 0.05 + 0.15x + 0.1y \end{pmatrix} \tag{33}$$

DOI: 10.1002/nme

Table I. Shape functions used for various element types.

Element Type	Type of shape function	Order of shape functions on the boundary
Q4	Lagrange shape functions	Linear
Q8	Serendipity shape functions (c.f. Section 3.2)	Quadratic
H8	Lagrange shape functions	Linear
Poly2D (linear)	Wachspress interpolants	Linear
Poly2D (quadratic)	Serendipity shape functions (c.f. Section 3.2)	Quadratic
Poly3D	Wachspress interpolants	Linear

Table II. Error in the L^2 norm and H^1 seminorm for the two-dimensional linear patch test.

Mesh	CS-Poly2D (linear)		LS-Poly2D (linear)	
	L^2	H^1	L^2	H^1
a	1.7334×10^{-07}	2.3328×10^{-05}	5.3835×10^{-14}	2.8388×10^{-11}
b	1.6994×10^{-07}	3.4094×10^{-05}	1.9255×10^{-13}	4.4373×10^{-11}
c	7.2017×10^{-07}	2.2573×10^{-04}	2.0030×10^{-13}	7.0017×10^{-11}
d	7.4144×10^{-07}	2.5773×10^{-04}	2.9567×10^{-13}	1.0199×10^{-10}

Table III. Error in the L^2 norm and H^1 seminorm for the three-dimensional linear patch test.

Mesh	LS-H8		Mesh	LS-Poly3D	
	L^2	H^1	(c.f. Figure 8)	L^2	H^1
2×2×2	2.5242×10^{-16}	2.4820×10^{-12}	a	2.0280×10^{-12}	3.3428×10^{-10}
4×4×4	7.9454×10^{-16}	4.9945×10^{-12}	b	1.9218×10^{-12}	1.7529×10^{-10}
8×8×8	2.9384×10^{-16}	1.0012×10^{-12}	c	2.6660×10^{-12}	4.9320×10^{-10}
16×16×16	8.9235×10^{-16}	2.0093×10^{-12}	d	3.2074×10^{-12}	3.1083×10^{-10}

and in the three-dimensional case the following displacements are prescribed on the boundary:

$$\begin{pmatrix}\hat{u}\\ \hat{v}\\ \hat{w}\end{pmatrix} = \begin{pmatrix}0.1+0.1x+0.2y+0.2z\\ 0.05+0.15x+0.1y+0.2z\\ 0.05+0.1x+0.2y+0.2z\end{pmatrix}. \tag{34}$$

The exact solution to Equation (1) is $\mathbf{u}=\hat{\mathbf{u}}$ in the absence of body forces. The domain is discretized with arbitrary polygonal and polyhedral finite elements. Figure 7 shows a few representative meshes used for the two-dimensional study and Figure 8 shows a few representative meshes used for the three-dimensional study. The performance of the linear smoothing over hexahedral elements is also studied using a structured mesh (2×2×2, 4×4×4, 8×8×8 and 16×16×16). The errors in the L^2 norm and H^1 seminorm for the CS and LS schemes are shown in Table II for two-dimensions and in Table III for three dimensions. It can be seen that the proposed LS scheme passes the linear patch test to machine precision for both polygonal and polyhedral discretizations, contrary to the linear smoothing as shown in [2].

5.2. *Quadratic patch test*

In the quadratic patch test, the following displacements are prescribed on the boundaries for the two-dimensional case:

$$\begin{pmatrix}\hat{u}\\ \hat{v}\end{pmatrix} = \begin{pmatrix}0.1x^2+0.1xy+0.2y^2\\ 0.05x^2+0.15xy+0.1y^2\end{pmatrix}, \tag{35}$$

DOI: 10.1002/nme

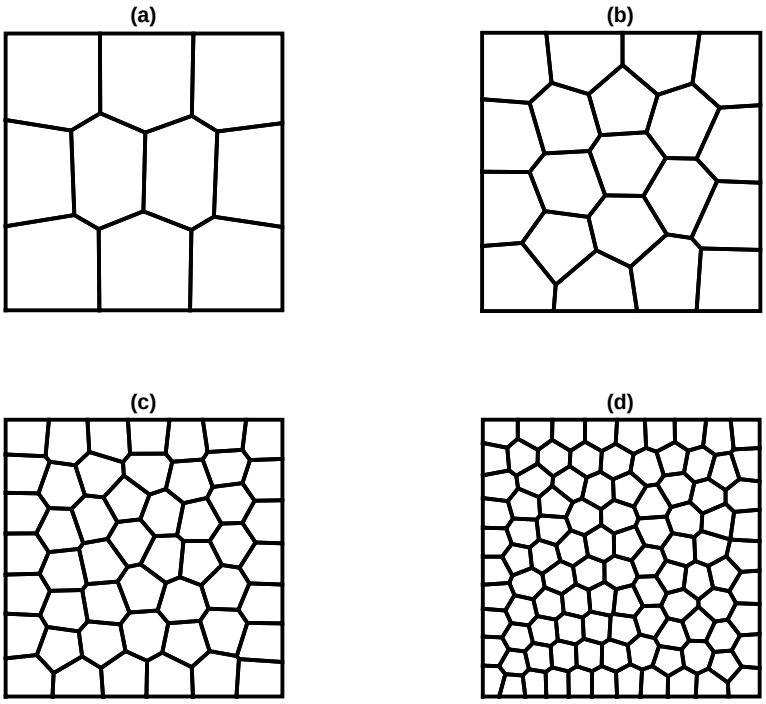

Figure 7. Square domain discretized with polygonal elements. Representative meshes containing (a) 10, (b) 20, (c) 50 and (d) 100 polygons.

and the following in the three-dimensional case:

$$\begin{pmatrix} \hat{u} \\ \hat{v} \\ \hat{w} \end{pmatrix} = \begin{pmatrix} 0.1 + 0.2x + 0.2x + 0.1z + 0.15x^2 + 0.2y^2 + 0.1z^2 + 0.15xy + 0.1yz + 0.1zx \\ 0.15 + 0.1x + 0.1y + 0.2z + 0.2x^2 + 0.15y^2 + 0.1z^2 + 0.2xy + 0.1yz + 0.2zx \\ 0.15 + 0.15x + 0.2y + 0.1z + 0.15x^2 + 0.1y^2 + 0.2z^2 + 0.1xy + 0.2yz + 0.15zx \end{pmatrix}. \tag{36}$$

The exact solution to Equation (1) is $\mathbf{u} = \hat{\mathbf{u}}$ when the body is subjected to the body forces:

$$\mathbf{b} = \begin{pmatrix} -0.2\mathbf{C}(1,1) - 0.15\mathbf{C}(1,2) - 0.55\mathbf{C}(3,3) \\ -0.1\mathbf{C}(1,2) - 0.2\mathbf{C}(2,2) - 0.2\mathbf{C}(3,3) \end{pmatrix}, \tag{37}$$

in two-dimensions and

$$\mathbf{b} = \begin{pmatrix} -0.3\mathbf{C}(1,1) - 0.2\mathbf{C}(1,2) - 0.15\mathbf{C}(1,3) - 0.6\mathbf{C}(4,4) - 0.35\mathbf{C}(6,6) \\ -0.15\mathbf{C}(1,2) - 0.3\mathbf{C}(2,2) - 0.2\mathbf{C}(2,3) - 0.55\mathbf{C}(4,4) - 0.4\mathbf{C}(5,5) \\ 0.1\mathbf{C}(1,3) - 0.1\mathbf{C}(2,3) - 0.4\mathbf{C}(3,3) - 0.3\mathbf{C}(5,5) - 0.4\mathbf{C}(6,6) \end{pmatrix}. \tag{38}$$

in three dimensions, where $\mathbf{C}$ is the constitutive matrix. For the quadratic patch test, the domain is discretized with arbitrary polyhedral elements. The number of elements is kept the same as for the linear patch test (Figures 7 - 8). The additional difference (in two-dimensions) is that for the quadratic patch test additional mid-side nodes are added and quadratic serendipity shape functions are used to represent the unknown fields. Table IV shows the relative error in the L^2 norm and H^1 seminorm for both LS-Poly2D (linear) and LS-Poly2D (quadratic) elements. The quadratic elements pass the quadratic patch test to machine precision, and the linear elements asymptotically converge with optimal convergence rates in the L^2 norm and H^1 seminorm as shown in Figure 9. Figure 10

DOI: 10.1002/nme

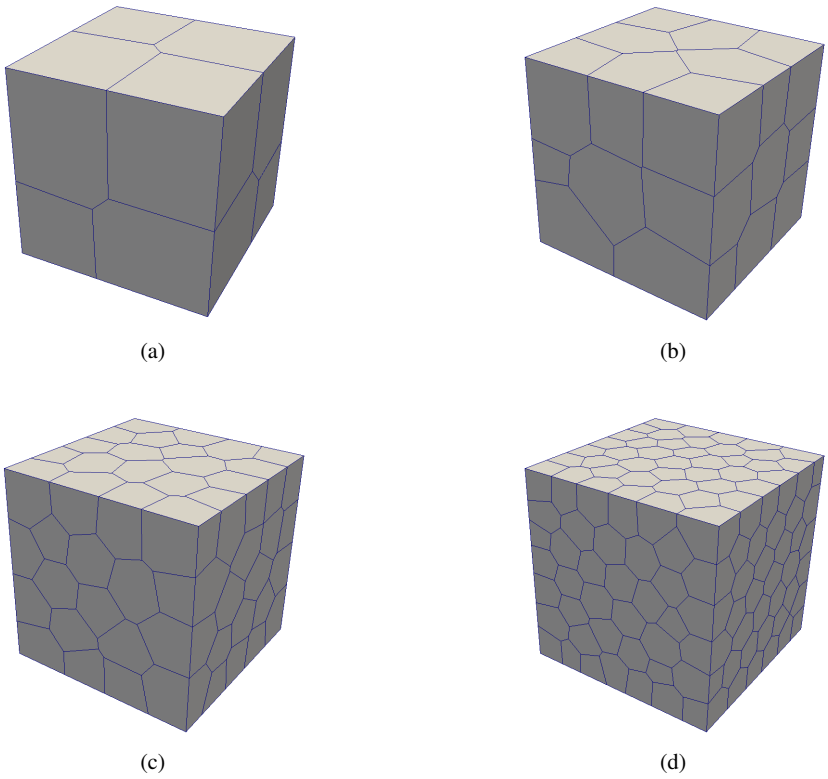

Figure 8. Representative polyhedral meshes for the linear and quadratic patch tests containing: (a) 10, (b) 20, (c) 100 and (d) 300 polygons.

Table IV. Error in the L^2 norm and H^1 seminorm for the two-dimensional quadratic patch test.

Mesh	LS-Poly2D (linear)		LS-Poly2D (quadratic)	
	L^2	H^1	L^2	H^1
a	3.3983×10^{-02}	11.478×10^{-01}	1.1136×10^{-13}	1.6919×10^{-11}
b	1.7769×10^{-02}	8.4327×10^{-01}	1.2054×10^{-13}	2.3663×10^{-11}
c	6.3758×10^{-03}	5.2839×10^{-01}	1.4929×10^{-13}	3.9634×10^{-11}
d	3.6644×10^{-03}	3.8407×10^{-01}	2.6857×10^{-13}	7.1208×10^{-11}

shows the convergence rates when the domain is discretized with the linear smoothed hexahedral and polyhedral linear elements. It can be inferred that the linear smoothing operation yields optimal convergence rates.

To study the effect of mesh distortion, we consider the higher order patch test described in (c.f Chapter 10, Sec. 10.7 [38]). The domain is discretized with two 8-noded quadrilateral elements. A state of plane stress is considered. The beam is subjected to a bending load as shown in Figure 11. The results are tabulated in Table V for points A and B (see Figure 11 for the location of points). From the table, it can be observed that the accuracy of the conventional 8-noded element deteriorates rapidly with increased distortion. It was observed in [1] that the conventional smoothing technique (constant smoothing) failed to pass the higher order patch test, even with 16 subcells. This could be attributed to the inaccurate computation of the smoothed derivatives. However, the 8-noded element with quadratic serendipity shape functions described in Section 3 and with the proposed integration scheme passes the higher order patch test. It can also be seen that the results are insensitive to the

DOI: 10.1002/nme

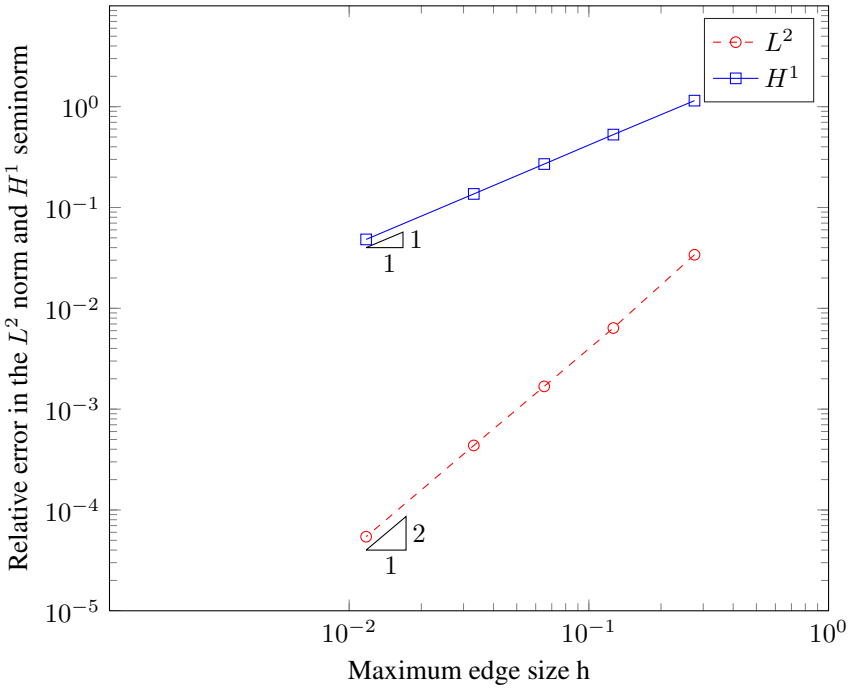

Figure 9. Convergence results for the quadratic patch test when the domain is discretized with LS-Poly2D (linear) elements. The LS scheme delivers optimal convergence rates in both the L^2 norm and H^1 seminorm.

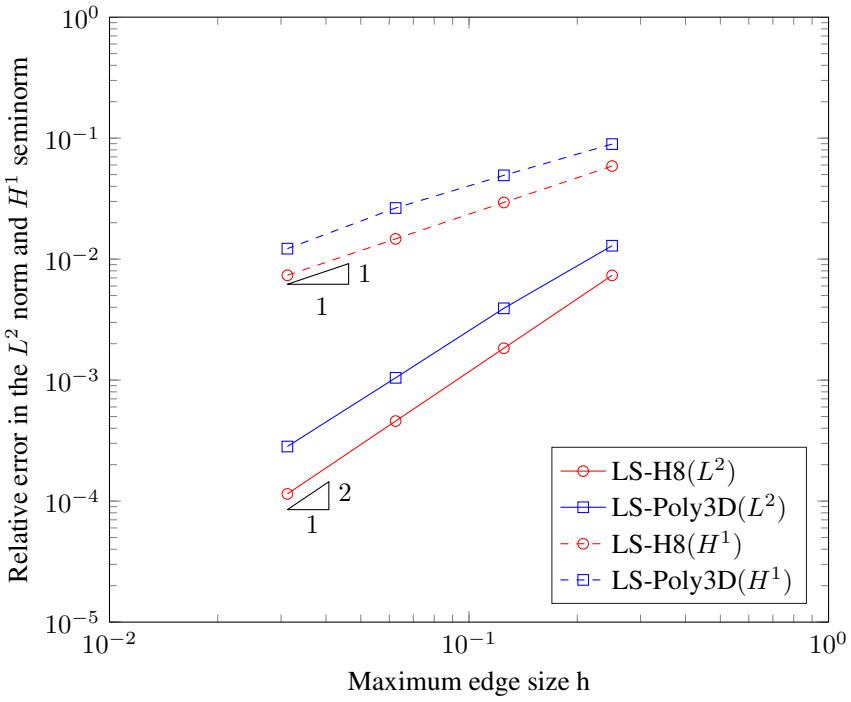

Figure 10. Convergence results for the quadratic patch test when the domain is discretized with the linear smoothed polyhedral and hexahedral elements. The scheme yields optimal convergence rates for hexahedral and polyhedral elements.

DOI: 10.1002/nme

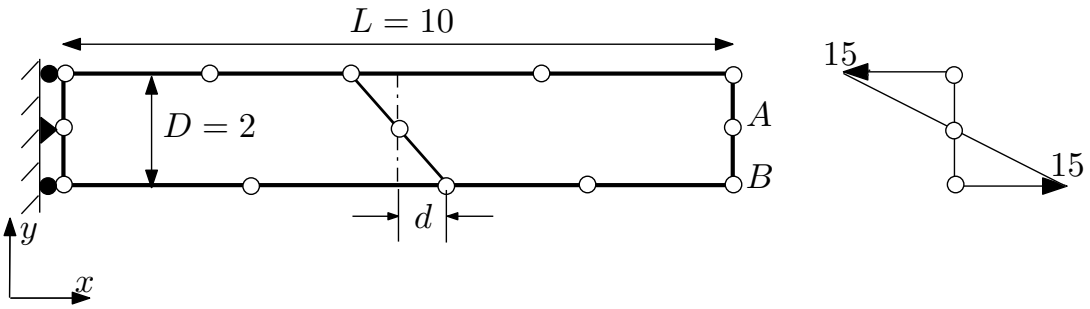

Figure 11. Patch test for 8- noded isoparametric elements.

Table V. Higher order patch test. v_A is the displacement at point A in the $y-$ direction and u_B, v_B are the displacements at point B along the $x-$ and $y-$ direction, respectively.

Method	Quadrature rule	subcells	d	v_A	u_B	v_B
Exact	-	-	-	0.75	0.15	0.75225
FEM	3×3	-	0	0.74999	0.14999	0.75225
	3×3	-	1	0.74999	0.14999	0.74572
	2×2	-	2	0.6684	0.1333	0.66364
CS-Q8 [1]	-	1	0	1.0000	0.20000	1.0030
	-	4	0	0.8438	0.16875	0.8462
	-	16	0	0.7813	0.1562	0.7836
LS-Q8	-	-	0	0.75	0.15	0.75225
	-	-	1	0.75	0.15	0.75225
	-	-	2	0.75	0.15	0.75225
Q8 (serendipity shape functions)	3 per triangle	-	1	0.74979	0.1499	0.7519
	7 per triangle	-	1	0.7499	0.1499	0.7255
	20 per triangle	-	1	0.75	0.15	0.75230

distortion parameter d. The table also presents the results, when the quadratic serendipity element is integrated by sub-triangulation employing triangular quadrature. It can be seen that the sub-triangulation requires more integration points to get the same level of accuracy as that of LS-Q8.

5.3. Two-dimensional cantilever beam under parabolic end load

In this example, a two-dimensional cantilever beam subjected to a parabolic shear load at the free end is examined, as shown in Figure 12. The geometry of the cantilever is $L = 10$ m and $D = 2$ m. The material properties are: Young's modulus, $E = 3\times10^7$ N/m^2, Poisson's ratio $\nu = 0.25$ and the parabolic shear force is $P = 150$ N. The exact solution for the displacement field is given by:

$$u(x,y) = \frac{Py}{6EI}\left[(9L-3x)x + (2+\nu)\left(y^2 - \frac{D^2}{4}\right)\right],$$
$$v(x,y) = -\frac{P}{6EI}\left[3\nu y^2(L-x) + (4+5\nu)\frac{D^2x}{4} + (3L-x)x^2\right]. \quad (39)$$

where $I = D^3/12$ is the second area moment. A state of plane stress is considered. Figure 13 shows sample polygonal meshes. The numerical convergence of the relative error in the L^2 norm and H^1 seminorm is shown in Figure 14. The results from the conventional polygonal finite element method (PFEM) is also presented. For the PFEM, sub-triangulation approach with higher order quadrature rule (13 points per triangle) is employed to integrate the terms in the stiffness matrix. It can be seen that the proposed linear smoothing scheme yields the optimal convergence rate in both the L^2

DOI: 10.1002/nme

norm and the H^1 seminorm. With mesh refinement the solution approaches the analytical solution asymptotically.

Finally, a 4-noded structured quadrilateral mesh is used to discretize the beam domain and the CS-Q4 and LS-Q4 elements are tested. Four subcells within each Q4 element when the CS scheme is used, while the smoothing function $f(x_1, x_2) = [1 \;\; x_1 \;\; x_2 \;\; x_1 x_2]^{\mathrm{T}}$ is used for the LS scheme, which eliminates the subcells that otherwise would be required [10]. Figure 15 shows the convergence rates for the two-dimensional cantilever beam when the CS-Q4 and LS-Q4 elements are used. It can be inferred from Figure 15 that the proposed LS scheme on the Q4 element delivers rates and accuracy that are comparable to the CS scheme with subcells on the same Q4 element.

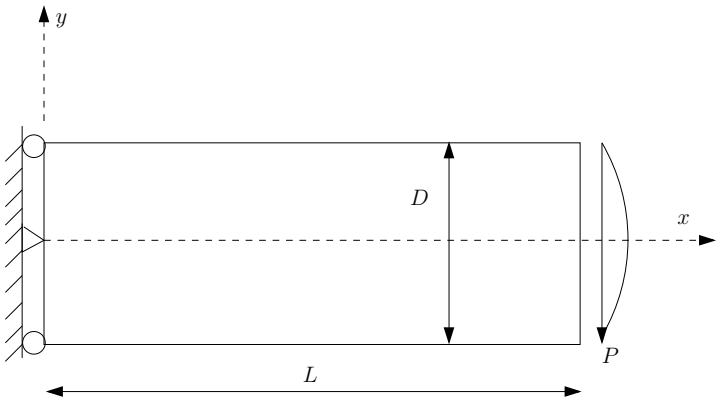

Figure 12. Geometry and boundary conditions for the two dimensional cantilever beam problem.

5.4. Three-dimensional cantilever beam under shear end load

In this example, a three-dimensional cantilever beam under shear load at the free end is studied. Figure 16(a) presents the schematic view of the problem. The domain Ω for this problem is $[-1, 1] \times [-1, 1] \times [0, L]$. The material is assumed to be isotropic with Young's modulus, $E = 1$ N/m^2 and Poisson's ratio $\nu = 0.3$. The beam is subjected to a shear force F at $z = 0$ and at any cross section of the beam, we have:

$$\int_{-a}^{b}\int_{-a}^{b} \sigma_{yz} \, \mathrm{d}x\mathrm{d}y = F,$$
$$\int_{-a}^{b}\int_{-a}^{b} \sigma_{zz} y \, \mathrm{d}x\mathrm{d}y = Fz. \tag{40}$$

The Cauchy stress field is given by [39]:

DOI: 10.1002/nme

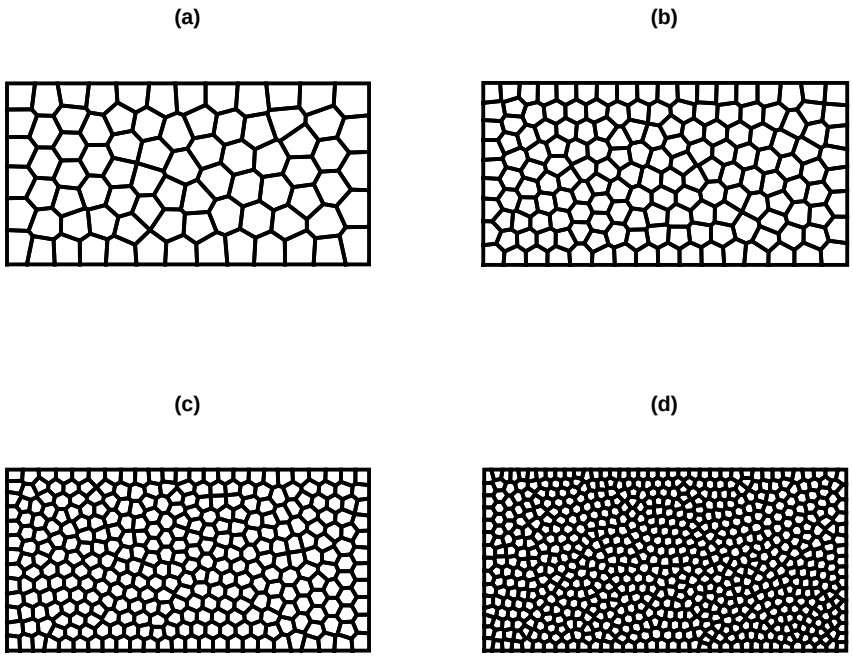

Figure 13. Sample meshes for the two dimensional cantilever beam problem containing: (a) 80, (b) 160, (c) 320 and (d) 640 polygons.

$$\sigma_{xx}(x,y,z) = \sigma_{xy}(x,y,z) = \sigma_{yy}(x,y,z) = 0; \quad \sigma_{zz}(x,y,z) = \frac{F}{I}yz; \tag{41}$$

$$\sigma_{xz}(x,y,z) = \frac{2a^2\nu F}{\pi^2 I(1+\nu)} \sum_{n=0}^{\infty} \frac{(-1)^n}{n^2} \sin\left(\frac{n\pi x}{a}\right) \frac{\sinh\left(\frac{n\pi y}{a}\right)}{\cosh\left(\frac{n\pi b}{a}\right)}$$

$$\sigma_{yz}(x,y,z) = \frac{(b^2-y^2)F}{2I} + \frac{\nu F}{I(1+\nu)} \left[\frac{3x^2-a^2}{6} - \frac{2a^2}{\pi^2} \sum_{n=1}^{\infty} \frac{(-1)^n}{n^2} \cos\left(\frac{n\pi x}{a}\right) \frac{\cosh\left(\frac{n\pi y}{a}\right)}{\cosh\left(\frac{n\pi b}{a}\right)}\right]. \tag{42}$$

The corresponding displacement field [40]:

$$u(x,y,z) = -\frac{\nu F}{EI}xyz; \quad v(x,y,z) = \frac{F}{EI}\left[\frac{\nu(x^2-y^2)z}{2} - \frac{z^3}{6}\right];$$

$$w(x,y,z) = \frac{F}{EI}\left[\frac{y(\nu x^2+z^2)}{2} + \frac{\nu y^3}{6} + (1+\nu)\left(b^2 y - \frac{y^3}{3}\right) - \frac{\nu a^2 y}{3} - \frac{4\nu a^3}{\pi^3} \sum_{n=0}^{\infty} \frac{(-1)^n}{n^2} \cos\left(\frac{n\pi x}{a}\right) \frac{\sinh\left(\frac{n\pi y}{a}\right)}{\cosh\left(\frac{n\pi b}{a}\right)}\right]. \tag{43}$$

where E is the Young's modulus, ν Poisson's ratio and $I = 4ab^3/3$ is the second moment of area about the x-axis. Two types of meshes are considered: (1) a regular hexahedral mesh and (2) a random closed-pack Voronoi mesh. Four levels of mesh refinement are considered for both the hexahedral mesh ($2\times2\times10$, $4\times4\times20$, $8\times8\times40$, $16\times16\times80$) and the random Voronoi mesh. A representative structured hexahedral mesh is presented in Figure 16(b) and Figure 17 depicts the random Voronoi meshes. The length of the beam is $L = 5$ m and the shear load is taken as $F = 1$ N. Analytical displacements given by Equation (43) are applied on the beam face at $z = L$ and

DOI: 10.1002/nme

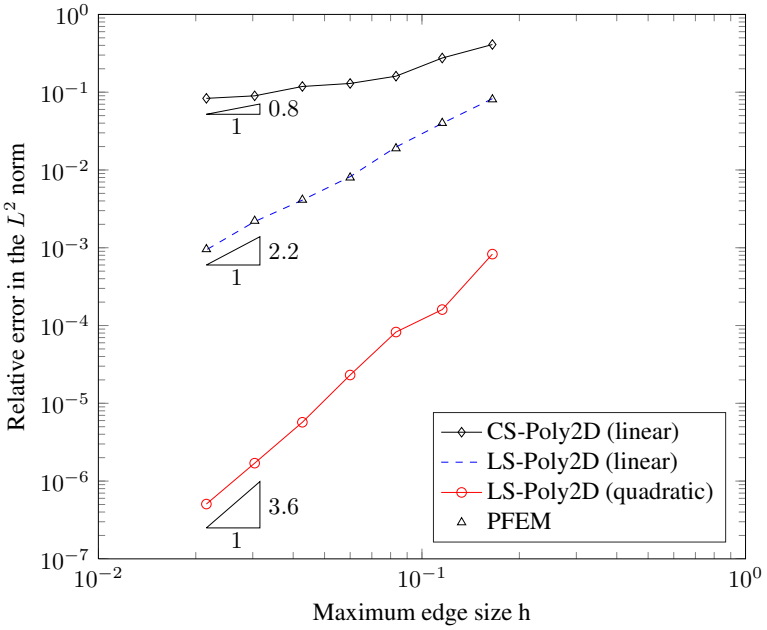

(a)

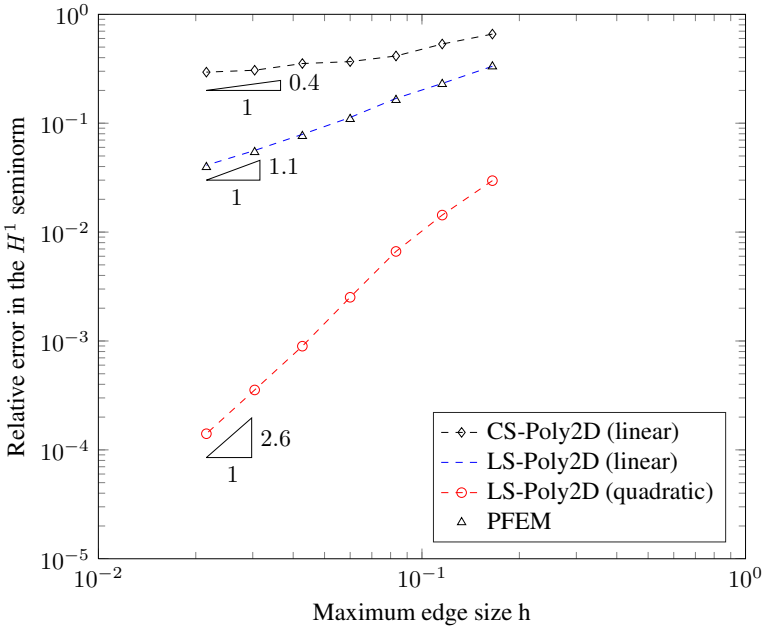

(b)

Figure 14. Convergence results for the two dimensional cantilever beam problem: relative error in the: (a) L^2 norm and (b) H^1 seminorm. We note that the LS scheme delivers optimal convergence rates for linear and quadratic elements.

the beam is loaded in shear on its face at $z = 0$. All other faces are assumed to be traction free. Figure 18 shows the relative error in the L^2 norm and H^1 seminorm with mesh refinement. It can be seen that the LS over hexahedral and polyhedral elements converges asymptotically with mesh refinement and delivers optimal convergence rates.

DOI: 10.1002/nme

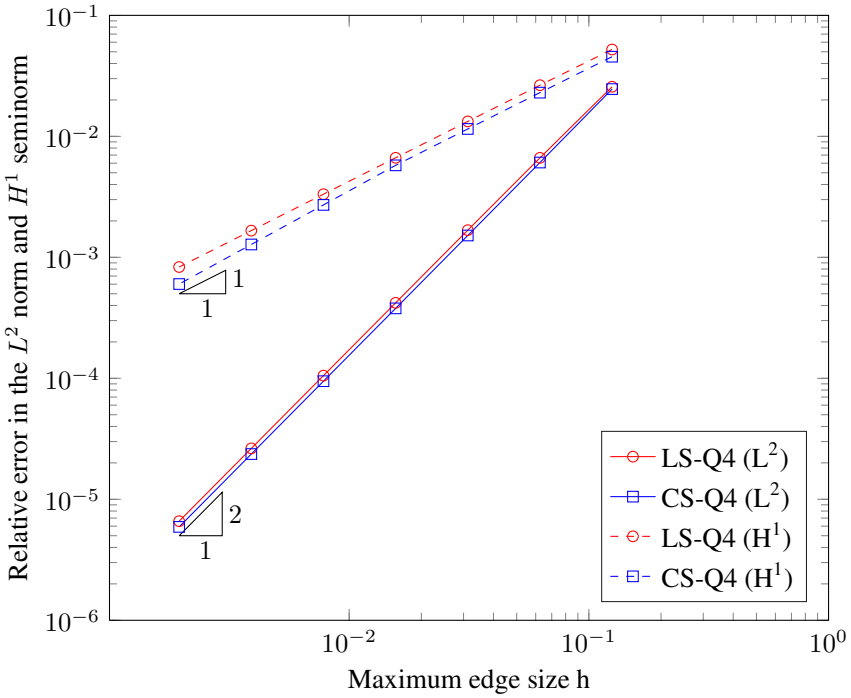

Figure 15. Convergence results for the cantilever beam subjected to end shear when the domain is discretized with constant and linear smoothed Q4 finite elements. The LS-Q4 delivers optimal convergence rates in both the L^2 norm and H^1 seminorm and the results are comparable with the results obtained with CS-Q4 with subcells.

5.5. Thick-walled cylinder subjected to internal pressure

In this example, consider a thick-walled cylinder subjected to internal pressure P. The internal and external radius of the cylinder are denoted by as a and b, respectively. Due to symmetry, only one quarter of the cylinder is modelled as shown in Figure 19. In the numerical computations, the following parameters are chosen: $a = 1$m, $b = 5$m and internal pressure $P = 3\times10^4$ N/m^2. The exact solution for this problem is now given. For a point $(x, y), r = \sqrt{x^2 + y^2}$, the radial and tangential displacements are given by

$$u_r(r) = \frac{a^2 Pr}{E(b^2 - a^2)}\left[(1-\nu) + \frac{b^2}{r^2}(1+\nu)\right],$$
$$u_\theta = 0. \tag{44}$$

A state of plate stress is assumed, and under this assumption, the strain components are only functions of the radius r and given by:

$$\varepsilon_r(r) = \frac{a^2 P}{E(b^2 - a^2)}\left[(1-\nu) - \frac{b^2}{r^2}(1+\nu)\right],$$
$$\varepsilon_\theta(r) = \frac{a^2 P}{E(b^2 - a^2)}\left[(1-\nu) + \frac{b^2}{r^2}(1+\nu)\right],$$
$$\varepsilon_{r\theta} = 0. \tag{45}$$

Figure 20 shows a few representative polygonal meshes used in the study. A convergence study is carried out using these discretizations and the convergence of the relative error in the L^2 norm and H^1 seminorm are shown in Figure 21 for both linear and quadratic polygonal elements with constant and linear smoothing scheme. It can be seen from this figure that linear smoothing yields optimal

DOI: 10.1002/nme

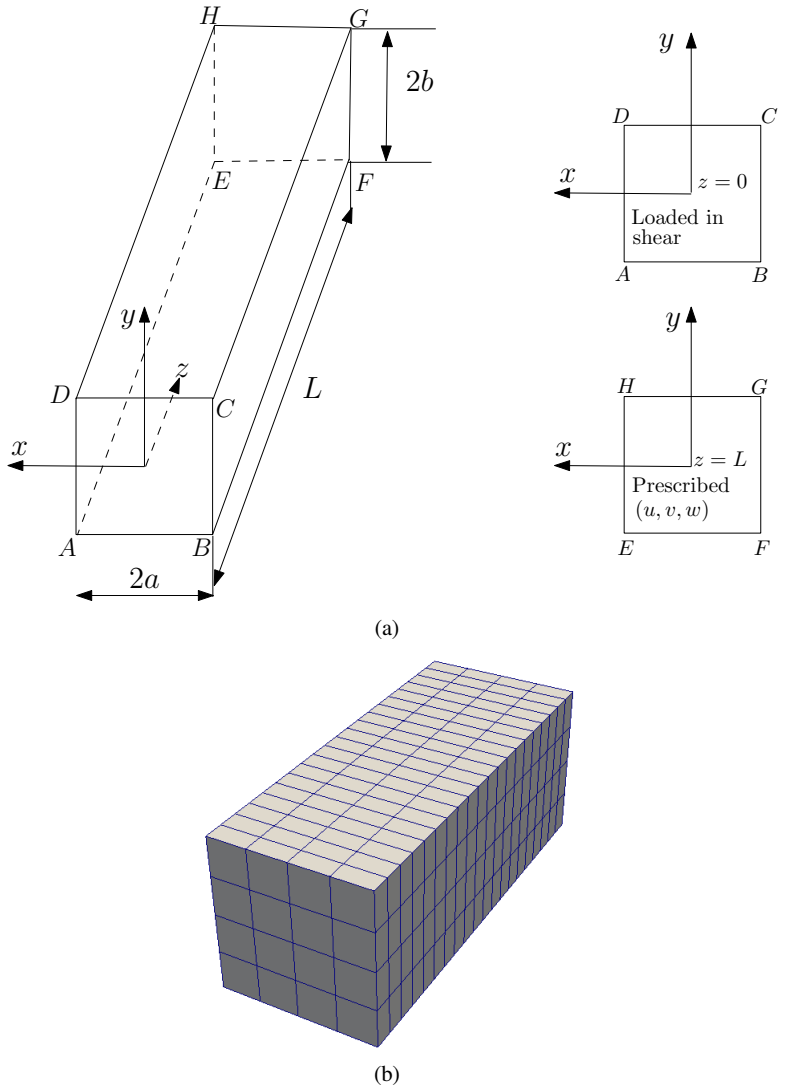

Figure 16. Three-dimensional cantilever beam problem: (a) Geometry and boundary conditions and (b) representative structured hexahedral mesh (4×4×20).

convergence rates for both linear and quadratic elements. Next, we discretize the domain with structured 4-noded quadrilateral elements and use $f(x_1, x_2) = [1 \;\; x_1 \;\; x_2 \;\; x_1 x_2]^{\mathrm{T}}$ as the smoothing function to eliminate the subcells that are required in the conventional SFEM [10]. The convergence of the relative error in the L^2 norm and H^1 seminorm is shown in Figure 22. It can be seen that the proposed LS scheme yields optimal convergence in both the the L^2 norm and the H^1 seminorm. It can also be deduced that the results of the LS-Q4 element are comparable with those of the CS-Q4 element with subcells.

6. CONCLUSIONS

In this paper, we presented a linear strain smoothing scheme for bilinear and bi-quadratic two-dimensional polygonal elements. We also extended the linear smoothing scheme to three-dimensional trilinear hexahedral and arbitrary polyhedral elements. The computation of corrected derivatives involves solving a small system of equations (Equation (28)). This slightly increases the

DOI: 10.1002/nme

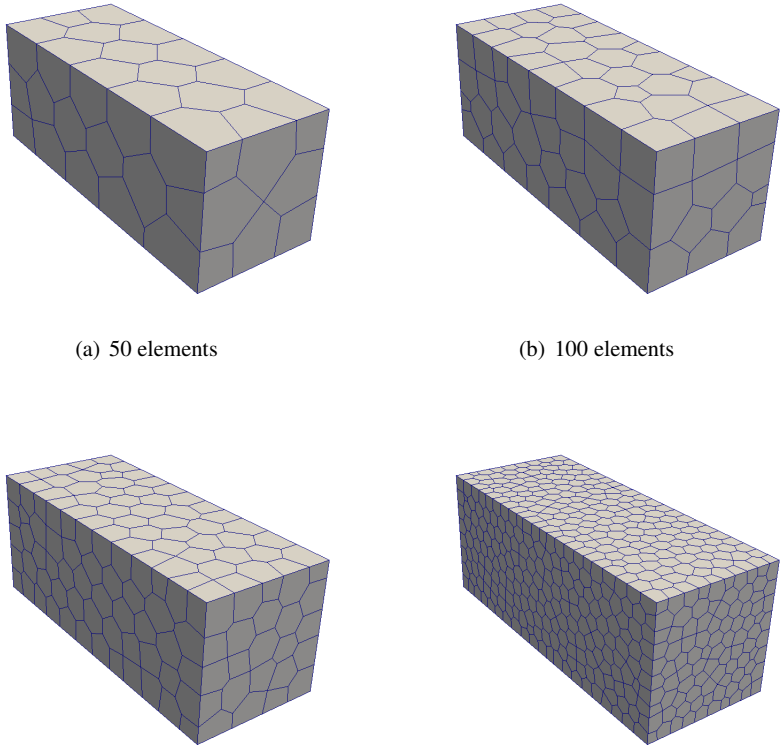

(a) 50 elements (b) 100 elements

(c) 300 elements (d) 2000 elements

Figure 17. Random closed-pack centroid Voronoi tessellation.

computational time when compared to constant smoothing technique. However, through numerical examples it was shown that the proposed smoothing scheme achieves accurate results and passes the patch test to machine precision in two and three dimensions. The results with linear smoothing technique is more accurate than the constant smoothing technique for arbitrary polytopes. It was also shown that for the Q4 element, with 'bilinear' smoothing function, the results from the proposed smoothing technique are similar to the constant smoothing technique with four subcells. The extension of quadratic serendipity elements to arbitrary polyhedra and its use within the linear smoothing technique is in progress and will be a topic of future communication.

ACKNOWLEDGEMENT

Stéphane Bordas would like to thank the support from the European Research Council Starting Independent Research Grant (ERC Stg grant agreement No. 279578) entitled "Towards real time multiscale simulation of cutting in non-linear materials with applications to surgical simulation and computer guided surgery as well as partial support from the EPSRC under grant EP/G042705/1 Increased Reliability for Industrially Relevant Automatic Crack Growth Simulation with the eXtended Finite Element Method and EP/I006494/1 Sustainable domain-specific software generation tools for extremely parallel particle-based simulations.

Simulations were supported by ARCCA and High Performance Computing (HPC) Wales, a company formed between the Universities and the private sector in Wales which provides the UKs largest distributed supercomputing network.

DOI: 10.1002/nme

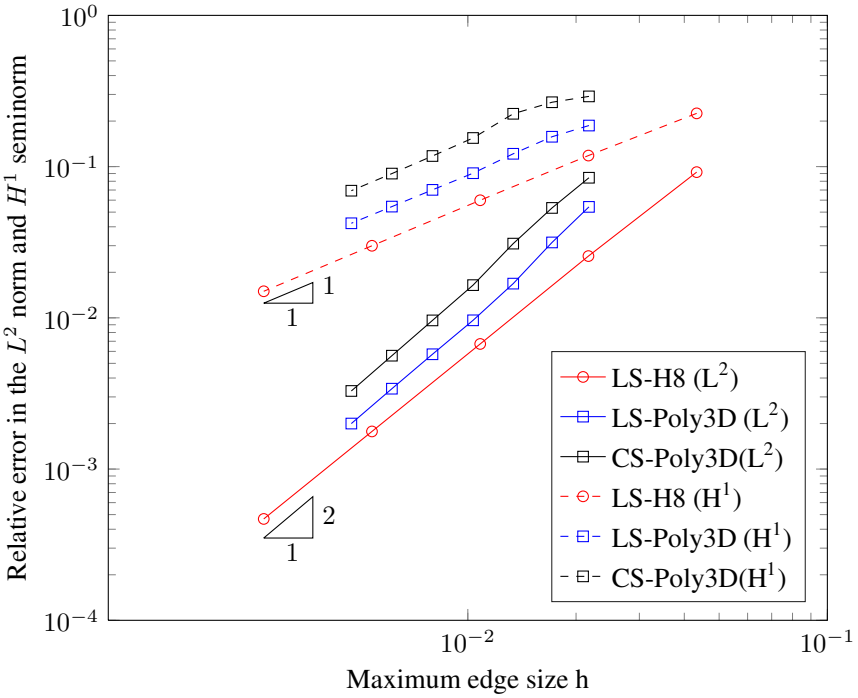

Figure 18. Convergence results for the three-dimensional cantilever beam problem.

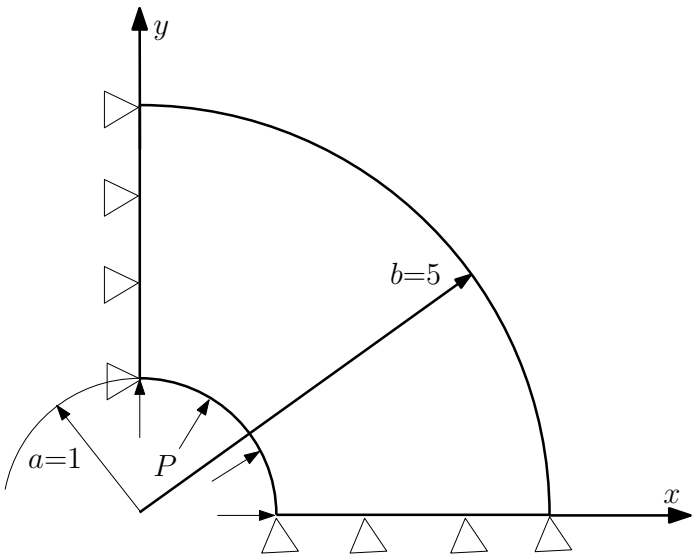

Figure 19. Thick-walled cylinder subjected to internal pressure.

A. QUADRATURES FOR THE LINEAR SMOOTHING SCHEME

The quadratures given here ensure invertibility of $\mathbf{W}$ in Equation (28). For a triangular cell, the following 3-point rule is used for the interior Gauß points:

$$\mathbf{T} = \begin{bmatrix} 2/3 & 1/6 & 1/6 \\ 1/6 & 2/3 & 1/6 \\ 1/6 & 1/6 & 2/3 \end{bmatrix} \tag{46}$$

DOI: 10.1002/nme

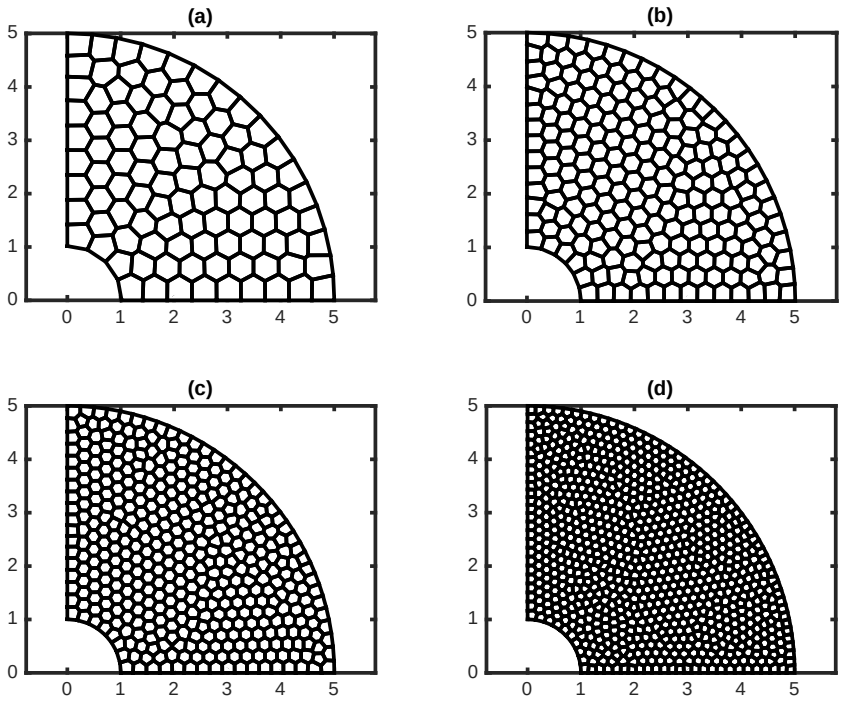

Figure 20. Representative meshes for the thick-walled cylinder containing: (a) 10, (b) 200 ,(c) 400 and (d) 800 polygons.

as the triangular coordinates, and

$$\mathbf{w} = \begin{bmatrix} 1/3 & 1/3 & 1/3 \end{bmatrix}^{\mathrm{T}} \tag{47}$$

as the corresponding weights; whereas the following 2-point rule for the edge Gauß points:

$$\xi = \begin{bmatrix} -0.57735026918962576450914878050 2 \\ 0.57735026918962576450914878050 2 \end{bmatrix} \tag{48}$$

as the normalized coordinates, and

$$\mathbf{v} = \begin{bmatrix} 1 & 1 \end{bmatrix}^{\mathrm{T}} \tag{49}$$

as the corresponding weights.

For a tetrahedral cell, the following 4-point rule is used for the interior Gauß points:

$$\mathbf{T} = \begin{bmatrix} 0.585410196624969 & 0.138196601125011 & 0.138196601125011 & 0.138196601125011 \\ 0.138196601125011 & 0.585410196624969 & 0.138196601125011 & 0.138196601125011 \\ 0.138196601125011 & 0.138196601125011 & 0.585410196624969 & 0.138196601125011 \\ 0.138196601125011 & 0.138196601125011 & 0.138196601125011 & 0.585410196624969 \end{bmatrix} \tag{50}$$

as the tetrahedral coordinates, and

$$\mathbf{w} = \begin{bmatrix} 1/4 & 1/4 & 1/4 & 1/4 \end{bmatrix}^{\mathrm{T}} \tag{51}$$

as the corresponding weights; whereas the 3-point rule that is used for the interior Gauß points of a triangular cell is employed for the face Gauß points of the tetrahedral cell.

DOI: 10.1002/nme

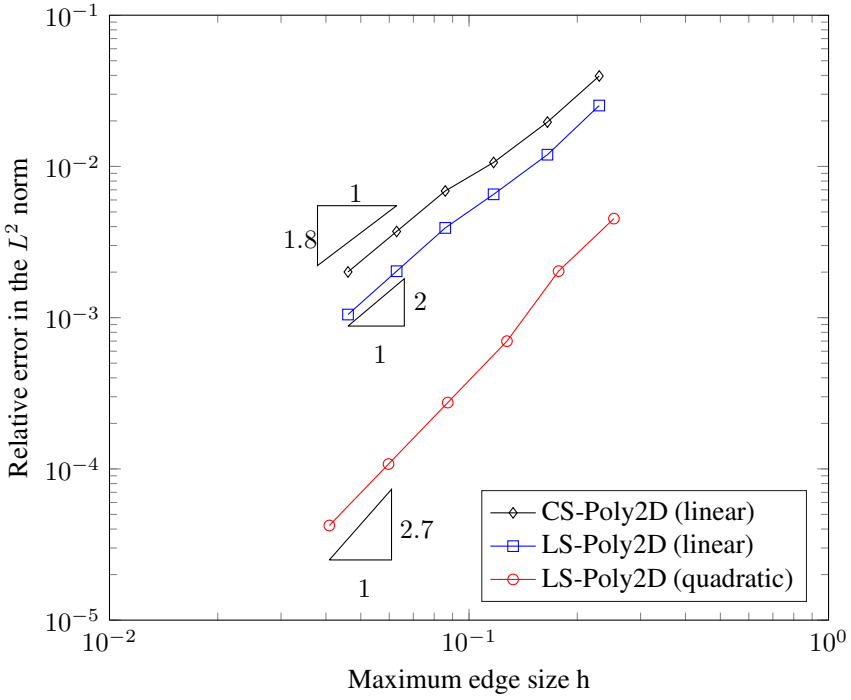

(a)

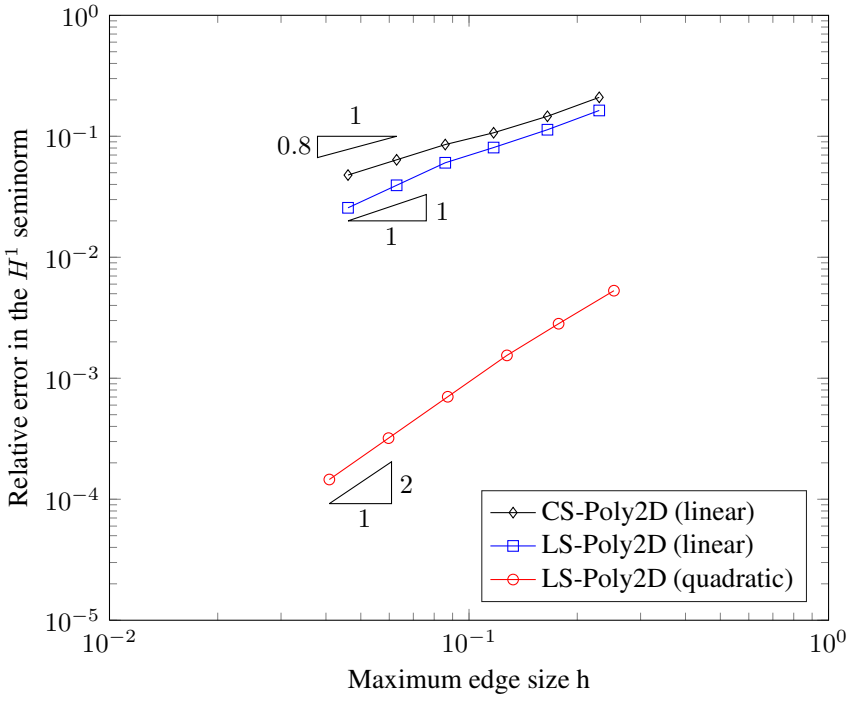

(b)

Figure 21. Convergence results for the thick-walled cylinder subjected to internal pressure when the domain is discretized with smoothed polygonal finite elements. We note that the LS-Poly2D (linear) and LS-Poly2D (quadratic) delivers optimal convergence rates.

DOI: 10.1002/nme

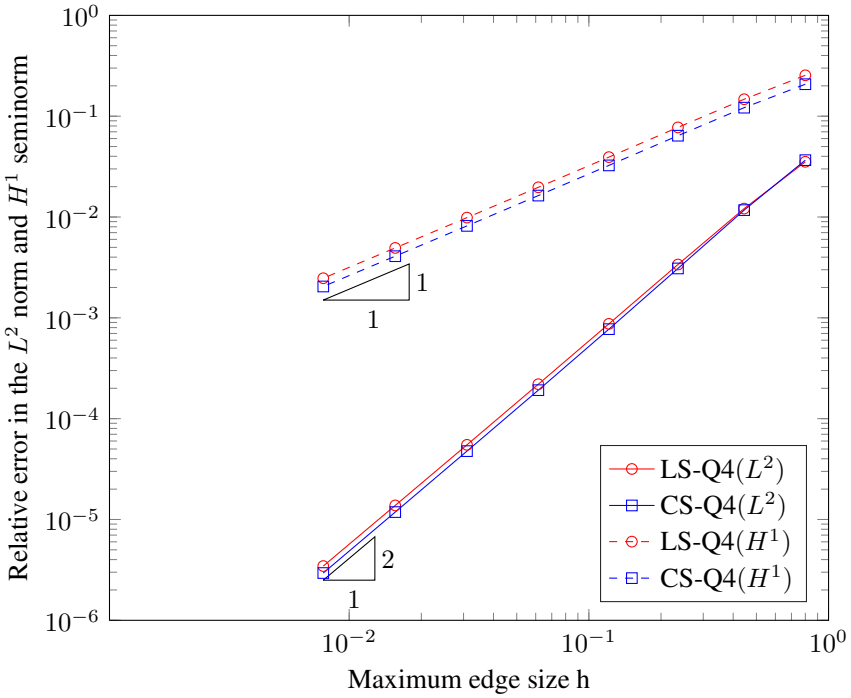

Figure 22. Convergence results for the thick-walled cylinder subjected to internal pressure when the domain is discretized with smoothed 4-noded quadrilateral elements. The results of the LS-Q4 are comparable with the results of the CS-Q4 element with subcells.

REFERENCES

1. Bordas S, Natarajan S, Kerfriden P, Augarde C, Mahapatra D, Rabczuk T, Pont S. On the performance of strain smoothing for quadratic and enriched finite element approximations (XFEM/GFEM/PUFEM). *International Journal for Numerical Methods in Engineering* 2011; **86**:637–666.
2. Natarajan S, Ooi ET, Chiong I, Song C. Convergence and accuracy of displacement based finite element formulation over arbitrary polygons: Laplace interpolants, strain smoothing and scaled boundary polygon formulation. *Finite Elements in Analysis and Design* 2014; **85**:101–122.
3. Chen JS, Wu CT, Yoon S, You Y. A stabilized conforming nodal integration for Galerkin mesh-free methods. *International Journal for Numerical Methods in Engineering* 2001; **50**(2):435–466.
4. Liu G, Dai K, Nguyen T. A smoothed finite elemen for mechanics problems. *Computational Mechanics* 2007; **39**:859–877.
5. Liu G, Nguyen T, Dai K, Lam K. Theoretical aspects of the smoothed finite element method (SFEM). *International Journal for Numerical Methods in Engineering* 2007; **71**(8):902–930.
6. Liu G, Nguyen-Thoi T, Nguyen-Xuan H, Lam K. A node based smoothed finite element (NS-FEM) for upper bound solution to solid mechanics problems. *Computers and Structures* 2009; **87**:14–26.
7. Liu G, Nguyen-Thoi T, Lam K. An edge-based smoothed finite element method (ES-FEM) for static, free and forced vibration analyses of solids. *Journal of Sound and Vibration* 2009; **320**:1100–1130.
8. Nguyen-Thoi T, Liu G, Lam K, Zhang G. A face-based smoothed finite element method (FS-FEM) for 3D linear and nonlinear solid mechanics using 4-node tetrahedral elements. *International Journal for Numerical Methods in Engineering* 2009; **78**:324–353.
9. Liu G, Nguyen-Thoi T, Lam K. A novel alpha finite element method (αfem) for exact solution to mechanics problems using triangular and tetrahedral elements. *Computer Methods in Applied Mechanics and Engineering* 2008; **197**:3883–3897.
10. Nguyen-Xuan H, Bordas S, Nguyen-Dang H. Smooth finite element methods: convergence, accuracy and properties. *International Journal for Numerical Methods in Engineering* 2008; **74**:175–208.
11. Nguyen-Xuan H, Rabczuk T, Bordas S, Debongnie J. A smoothed finite element method for plate analysis. *Computer Methods in Applied Mechanics and Engineering* 2008; **197**:1184–1203.
12. Nguyen-Thanh N, Rabczuk T, Nguyen-Xuan H, Bordas SP. A smoothed finite element method for shell analysis. *Computer Methods in Applied Mechanics and Engineering* 2008; **198**:165–177.
13. Ong TH, Liu G, Nguyen-Thoi T, Nguyen-Xuan H. Inf-Suf stable bES-FEM method for nearly incompressible elasticity 2013; URL http://arxiv.org/pdf/1305.0466.pdf.
14. Lee CK, Mihai LA, Kerfriden P, Bordas SP. The edge-based strain smoothing method for compressible and nearly incompressible non-linear elasticity for solid mechanics 2014; URL http://orbilu.uni.lu/bitstream/10993/14933/1/CKpaper.pdf.

DOI: 10.1002/nme

15. Bordas SP, Rabczuk T, Hung NX, Nguyen VP, Natarajan S, Bog T, Quan DM, Hiep NV. Strain smoothing in FEM and XFEM. *Computers & Structures* 2010; **88**:1419–1443.
16. Chen L, Rabczuk T, Bordas S, Liu G, Zheng K, Kerfriden P. Extended finite element method with edge-based strain smoothing (ESm-XFEM) for linear elastic crack growth. *Computer Methods in Applied Mechanics and Engineering* 2012; **209–212**:250–265.
17. Natarajan S, Bordas S, Ooi ET. Virtual and smoothed finite elements: a connection and its application to polygonal/polyhedral finite element methods. *International Journal for Numerical Methods in Engineering* 2015; doi:10.1002/nme.4965.
18. Beirão Da Veiga L, Brezzi F, Marini L. Virtual elements for linear elasticity problems. *SIAM Journal of Numerical Analysis* 2013; **51**:794–812.
19. Beirão Da Veiga L, Brezzi F, Marini L, Russo A. The Hitchhiker's Guide to the Virtual Element Method. *Mathematical models and methods in applied sciences* 2014; **24**:1541–1573.
20. Beirão Da Veiga L, Manzini G. A virtual element method with arbitrary regularity. *IMA Journal of Numerical Analysis* 2013; :1–23.
21. Gain AL, Talischi C, Paulino GH. On the Virtual Element Method for three-dimensional linear elasticity problems on arbitrary polyhedra meshes. *Computer Methods in Applied Mechanics and Engineering* 2014; doi:10.1016/j.cma.2014.05.005.
22. Dai K, Liu G, Nguyen T. An $n-$sided polygonal smoothed finite element method for solid mechanics. *Finite Elements in Analysis and Design* 2007; **43**:847–860.
23. Sukumar N, Tabarraei A. Conforming polygonal finite elements. *International Journal for Numerical Methods in Engineering* 2004; **61**:2045–2066.
24. Duan Q, Li X, Zhang H, Belytschko T. Second-order accurate derivatives and integration schemes for meshfree methods. *International Journal for Numerical Methods in Engineering* 2012; **92**(4):399–424.
25. Duan Q, Gao X, Wang B, , Li X, Zhang H, Belytschko T, Shao Y. Consistent element-free Galerkin method. *International Journal for Numerical Methods in Engineering* 2014; **99**(2):79–101.
26. Duan Q, Gao X, Wang B, Li X, Zhang H. A four-point integration scheme with quadratic exactness for three-dimensional element-free Galerkin method based on variationally consistent formulation. *Computer Methods in Applied Mechanics and Engineering* 2014; **280**(0):84–116.
27. Sukumar N, Malsch E. Recent advances in the construction of polygonal finite element interpolants. *Archives of Computational Methods in Engineering* 2006; **13**(1):129–163.
28. Bordas S, Natarajan S. On the approximation in the smoothed finite element method (SFEM). *International Journal for Numerical Methods in Engineering* 2010; **81**:660–670.
29. Wachspress E. *A rational basis for function approximation*. Springer, New York, 1971.
30. Meyer M, Lee H, Barr AH. Generalized barycentric coordinates for irregular n-gons. *Journal of Graphics Tools* 2002; **7**(1):13–22.
31. Warren J. On the uniqueness of barycentric coordinates. *Proceedings of AGGM02*, 2003; 93–99.
32. Warren J, Schaefer S, Hirani A, Desbrun M. Barycentric coordinates for convex sets. *Advances in Computational Mechanics* 2007; **27**(3):319–338.
33. Rand A, Gillette A, Bajaj C. Quadratic serendipity finite elements on polygons using generalized barycentric coordinates. *Mathematics of Computation* 2014; **83**:2691–2716.
34. Sukumar N. Quadratic maximum-entropy serendipity shape functions for arbitrary planar polygons. *Computer Methods in Applied Mechanics and Engineering* 2013; **263**:27–41.
35. Ortiz-Bernardin A, Hale JS, Cyron CJ. Volume-averaged nodal projection method for nearly-incompressible elasticity using meshfree and bubble basis functions. *Computer Methods in Applied Mechanics and Engineering* 2015; **285**:427–451.
36. Ortiz-Bernardin A, Puso MA, Sukumar N. Improved robustness for nearly-incompressible large deformation meshfree simulations on Delaunay tessellations. *Computer Methods in Applied Mechanics and Engineering* 2015; **293**:348–374.
37. Beirão Da Veiga L, Brezzi F, Cangiani A, Manzini G, Marini L, Russo A. Basic principles of virtual element methods. *Mathematical Models and Methods in Applied Sciences* 2013; **23**:199–214.
38. Zienkiewicz O, Taylor R. *The Finite element method*. Butterworth Heinemann, 2000.
39. Barber J. *Elasticity*. Springer, New York, 2010.
40. Bishop J. A displacement based finite element formulation for general polyhedra using harmonic shape functions. *International Journal for Numerical Methods in Engineering* 2014; **97**:1–31.